Nickel Doped Mn_3O_4 Nanoparticles: Synthesis, Characterization and Application as Photocatalyst

Master of Philosophy

In

Physical Chemistry

By

Kainat Shafqat

Department of Chemistry

Quaid-I-Azam University

Islamabad

(2023)

Nickel Doped Mn_3O_4 Nanoparticles: Synthesis, Characterization and Application as Photocatalyst

A dissertation submitted to the Department of Chemistry, Quaid-I-Azam University, Islamabad, in partial fulfillment of the requirement for the degree of

Master of Philosophy

In

Physical Chemistry

By

Kainat Shafqat

Department of Chemistry

Quaid-I-Azam University

Islamabad

(2023)

DECLARATION

This is to certify that this dissertation entitled **"Nickel Doped Mn_3O_4 Nanoparticles: Synthesis, Characterization and Application as Photocatalyst"** submitted by ***Ms. Kainat Shafqat,*** is accepted in its present form by the Department of Chemistry, Quaid-i-Azam University, Islamabad, as satisfying the dissertation requirements for the degree of ***Master of Philosophy in Physical Chemistry.***

External Examiner:

Dr. Habib Ahmad
Director
Chemical Safety Board
SPD North Chakalala Rawalpindi

Supervisor:

Prof. Dr. Syed Mujtaba Shah
Department of Chemistry
Quaid-i-Azam University
Islamabad

Head of Section:

Prof. Dr. Hazrat Hussain
Department of Chemistry
Quaid-i-Azam University
Islamabad

Chairman:

Prof. Dr. Aamer Saeed Bhatti
Department of Chemistry
Quaid-i-Azam University
Islamabad


بسم الله الرحمن الرحيم

Dedicated to the people I adore dearly, especially my devoted and supportive father Dr. Shafqat Rasool Zahid, my loving mother Ms. Badar Munir, my brothers Dr. Asad Rasool and Dr. Izn Ahmad and my husband Mr. Abubakar Khan.

Acknowledgment

Prayers be to Allah Almighty for showering His blessings on me throughout my research work and for His ultimate guidance.

I would like to acknowledge my deep and warm thanks to my supervisor **Prof. Dr. Syed Mujtaba Shah**, Department of Chemistry, Quaid-I-Azam University, Islamabad, for giving me the opportunity to work under his supervision. His knowledge, motivation and sincerity to his profession has deeply inspired me and it is his guidance that carried me through all the stages of my research work. I am very fortunate to perform my research under his supervision. I pay my special regards to the Chairman of the Chemistry Department **Prof. Dr. Amir Saeed Bhatti** for providing a healthy work environment and helping in this whole time.

I am extremely grateful to my parents and brothers for their unconditional love, support and valuable prayers. Specials thanks to them for believing in me and giving me this learning opportunity. I am also thankful to all teaching and non-teaching staff members of the department for their cooperative behavior during my research work.

I want to thank my friend **Humaira Khan** for continuously supporting and motivating me throughout my work. I would extent my gratitude to my seniors especially **Syed Naimat Ullah**, **Nasir Hussain** and **Yousaf Khan** for always giving me better ideas to carry out the research and encouraging me during my work. I am grateful to my junior lab fellows and class fellows for keeping a friendly environment and helping me in my work. I am also thankful to my friends **Tahseen Zafar**, **Tehseen Sadaqat**, **Eisha Ehsan**, **Bushra Asghar**, and **Maria Channa** for their care and moral support.

Finally, I would like to thank my husband **Abubakar Khan** for his constant affection and encouragement during the challenges of my research work. It was a blessing to have your prayers and love by my side.

Kainat Shafqat

Abstract

In the present research work, pristine and (1-4) % weighted percentage of Ni doped Mn_3O_4 nanoparticles were successfully synthesized followed by a co-precipitation method and characterized with UV-Visible spectroscopy, X-Ray powder diffraction (XRD), and Fourier transform infrared spectroscopy (FT-IR). UV-Visible spectroscopy was performed to find the optical properties of synthesized materials. It indicated that with an increase in Nickel percentage ranging from 1 to 3 % weighted percentage, a red shift was observed and with further increase in dopant percentage to 4 % weighted percentage, a decrease in wavelength was observed. Tauc plots of the synthesized nanoparticles showed tuning in band gap from 2.50 to 2.37 eV. XRD was done to check the purity and crystallinity of the materials. We found the average crystallite size through XRD technique. This analysis showed that the average crystallite size increases with increasing dopant percentage up to 3 % weighted percentage of Ni. For 4 % weighted percentage of Ni, a decrease was calculated. FT-IR was done for the functional group detection and vibrational study of synthesized materials. This study confirmed that the prepared samples were pure and showed vibrational bands of required samples. The application of synthesized nanoparticles was studied by using them as a catalyst for the degradation of dyes which are Methyl blue dye and Methyl orange dye. To find optimal conditions for both dyes, different parameters were checked which include percentage of dopant, dosage of catalyst, dye concentration and study of pH. Among all the catalysts, 3 mg dosage of 4 % Ni-Mn_3O_4 NPs showed maximum photodegradation efficiency (%PDE). 95.3 % of Methyl blue dye was degraded in 75 minutes at a basic pH 11 for 30 μM concentration of Methyl blue dye solution. Hence, Methyl blue was degraded by adsorbing it on the surface of prepared catalysts. The optimal conditions for 80 μM concentration of Methyl orange dye solution were found to be 2 mg amount of 2 % Ni-Mn_3O_4 NPs. 90 % of Methyl orange dye was degraded in 90 minutes under the optimal conditions. In order to remove organic pollutants from wastewater, photocatalysis is the most appealing and environment friendly chemical method. In this entire work, optimal conditions were found for the photocatalytic degradation of dyes in the presence of sunlight.

Table of contents

List of Figures

List of Tables

List of Abbreviations and Symbols

Symbols	Abbreviations
BOD	Biochemical oxygen demand
CB	Conduction band
(e^-/h^+)	Electron-hole pair
e^-	Electrons
E_g	Energy band gap
FT-IR	Fourier transform infrared spectroscopy
h^+	Holes
Max.	Maximum
MB	Methyl blue
MeO	Methyl orange
NPs	Nanoparticles
Ni-Mn_3O_4	Ni-doped manganese oxide
%PDE	Percentage degradation efficiency
SSA	Steady state approximation
VB	Valence band
XRD	X-Ray diffraction

CHAPTER 1: INTRODUCTION

1.1 Research background

Human beings affect the environment to serve their needs and take benefits from it. People always try to reconstruct new ecosystems that can better meet their demands. The availability of resources like water, fuel, wood, food, electricity, land, and many more are examples of ecosystem services that are very crucial for the survival of human beings. These resources have a large impact on the environment. That's how humans benefit the environment while also harming it in many ways. Technological advancement leads to the exploitation of natural resources by disrupting the natural cycles of biotic and abiotic ecosystems. Harmful substances released into the environment cause pollution, including air pollution, water pollution, land pollution, noise pollution, radioactive pollution, and many others. Water surrounds about 71% of the earth's surface, out of which 96.5% is existing in the oceans[1]. Clean water is very essential because it provides a habitat for organisms existing in water bodies. Water is in high demand as it helps raise the economy of a country. Major things like food, industries, manufacturing, tourism, farming, and the production of energy depend mostly on the availability of clean water. Only 1% of the water available for drinking purposes comes from rivers and streams.[2] The rest of the water is in the form of ice glaciers or trapped beneath the earth. With the increasing population, water pollution has become very common. Discharge of untreated waste, sewage line leaks, toxic chemicals from farms, organic and inorganic substances, dyes, and wastewater from industries without any treatment to eliminate toxic compounds results in water pollution. Industries are the major cause, as they release wastes into nearby water bodies. Among industries, the textile industry uses major water content. In 2015, the global textile and clothing sector is estimated to have used 79 billion cubic meters of water. Almost 20% of the clean water pollution in the world is due to the dyeing and finishing industries in the textile industry. It is estimated that worldwide, 80% of diseases and 50% of child mortality occur due to a lack of clean water.

Chemicals in dyes cause contamination of water, loss of aquatic life, crop damage, and many waterborne diseases. Dyes contain acidic and basic ions that get into water and decrease their transparency by decreasing the absorbance of light. In this way, the oxygen content of water drops which disturbs the rate of photosynthesis, the

growth of plants, and the habitat of many other organisms. The dyeing, printing, and finishing of products in the textile industry are largely responsible for variations in the quality of water and other parameters like pH, temperature, chemical oxygen demand (COD), biological oxygen demand (BOD), color, and salinity[3]. Because of the lack of pure water sources, there has been a lot of interest in treating dye wastewater, and degradable dyes are getting more use. An efficient way is to remove large amounts of dye rapidly without creating secondary pollutants.

The three primary kinds of conventional dye degradation techniques are physical, chemical, and biological techniques. Physical technique involves the removal of dispersed dyes by using reverse osmosis, microfiltration, and adsorption methods, but this method is expensive and desires high maintenance. Chemical technique is efficient in the removal of dyes from water but it also produces secondary chemical wastes. Biological technique is cost-effective and doesn't yield toxic byproducts, but it is not effective for synthetic dyes.

Therefore, it is essential to devise ways that can properly remove the pollutants. Advanced oxidation processes remove pollutants from wastewater and sewage leaks[4]. Based on irradiation, it includes homogeneous and heterogeneous methods, among which photocatalysis is the best choice. Photodegradation of dyes is ecofriendly and very cost effective. This thesis emphasis on the photocatalytic degradation of Methyl blue (MB) and Methyl orange (MeO) by transition metal Ni-Mn_3O_4 NPs. It also explains the synthesis, characterization, and kinetic rate of Mn_3O_4 nanoparticles.

1.2 Water pollution

The presence of excess harmful substances, mostly chemicals, in water bodies like lakes, rivers, and seas degrades the quality of the water and makes it destructive for living organisms and environment is known as water pollution. These harmful substances are called water pollutants.

1.3 Types of water pollution

Point source pollution and non-point source pollution are the two primary forms among the numerous sorts of water pollution sources.

1.3.1 Point source pollution

The pollution arising from contaminants coming from a single identifiable source is known as point source pollution. These pollutants can go into water surface or seep into the ground. The exact point of these pollutants is known, so we can measure the quantity and take the necessary actions to control this pollution[5]. Point source pollution originates from unnatural sources like industry, sewage, agriculture, and oil spillage.

1.3.2 Non-point source pollution

The pollution arising from contaminants that come from diffuse sources is known as non-point source pollution. This pollution spread over a vast range via various routes, and the precise source of these pollutants is difficult to pinpoint[6]. People contribute to this pollution without even knowing it. Non-point source pollution results from waste water coming from agricultural lands, fuels, acid rain, and urban areas.

1.4 Causes of water pollution

There are a lot of causes of water pollution out of which some are deliberated here.

1.4.1 Industrial waste

The major contribution to water pollution arises from industrial sites. Industries release many toxic chemicals without proper waste removal treatments. These wastes can be biodegradable or non-biodegradable. Biodegradable wastes decompose naturally and convert into harmless substances after some time, while non-biodegradable wastes cannot convert into nontoxic substances. Both of them have their own impact on disturbing the natural ecosystem.

Industrial waste includes heavy metals, insoluble salts, and plastic. The toxic chemicals can easily enter the environment and living organisms. The contaminated water enters into small water bodies (lakes, streams, rivers) and then into large water bodies (oceans, seas).

These chemicals degrade water structure and make water unfit for many habitats. Wastes or chemicals produce by various industries are written in Table 1.1[7].

Table 1.1: Different industries and their wastes released.

Industries	Wastes released
Energy	Ash, toxic gasses, boiler slag, particulates, solvents, used oils, slurry
Mining	Solid rock, waste rock, coal, slag, muds, mill tailings
Manufacturing	Catalysts, chemical solvents like benzene, reactive substances, acids, bases, used oils, ash, mud, organic compounds, heavy metals
Construction	Concrete, gypsum, asphalt, wood waste, petroleum distillates, solvents, slate, metals, glass, plaster, paints
Chemical	Wastes, solvents, dyes, acids and bases, organic and inorganic effluents
Leather	Hydrocarbons, organic dyes, petroleum, sulphides, waste water
Petrochemical	Harmful wastes of solvents, hydrocarbons
Transport	Petroleum, benzene, oils, heavy metals, alcohols, VOCs
Paper/printing	Ignitable solvents, paper trash, glazes, stripping compounds, solvents, paint residues, ink waste

1.4.2 Sewage and wastewater

Waste water from households generates sewage waste. The wastewater is treated chemically but sometimes enters untreated into freshwater bodies like seas and oceans. It contains many harmful pollutants, microorganisms, bacteria, and chemicals that cause health issues. The presence of pathogens in water makes it unfit for humans and animals and causes many diseases. Sewage and wastewater deteriorate the color of water and make it unhealthy for drinking purposes.

1.4.3 Agricultural waste

Agricultural waste also contributes to water pollution. Mostly farmers use chemicals, organic products, and pesticides to protect their crops from bacteria, insects, and other pests. These chemicals are water insoluble and potentially harmful for human health. They cannot be broken easily and take a lot of time. In this way, agricultural wastes remain undissolved and spoil water quality. Organic products seep into the ground and leave devastating effects on humans, animals, and plants. They flow with rainwater into rivers, lakes, and oceans, which leads to water pollution.

1.5 Overview of dyes

Dyes are used as coloring materials. Dyes are organic and can give color to textiles, photographs, paints, cosmetics, leather, food, and pharmaceutics. They can bind chemically and physically with a substrate and are easily soluble in a solvent. Till the mid-19th century, humans used natural dyes that originated from living sources. By the end of the 19th century, natural dyes were replaced by synthetic dyes due to their high pigmentation demands[8]. Dyes are different from pigments as they are mostly organic compounds, while pigments can be inorganic. Pigments are not soluble in a solvent medium and form suspensions.

Dyes that exhibit color in less time are considered good and stable dyes. Dyes give color due to the presence of some general characteristics like

- Close association with the substrate is necessary to impart even coloring and resistance to heat and light.
- Absorption of light in the UV-Visible region.
- Chemical interactions between substituents of the dye and fiber.
- A conjugated system with alternate single and double bonding in structure.
- Presence of a specific coloring group named the chromophore in the structure (Otto Witt, 1876).

Dyes cannot show color in the absence of these features. The main reason for color in dyes is chromophore, which includes nitro (-NO_2), carbonyl (-C=O), and nitroso (-NO) groups[9]. Witt theory suggests the presence of auxochromes on chromophores. Auxochromes are not directly involved in giving color to dyes. They support chromophores and modify their functions due to the existence of resonating, saturated,

and unsaturated bonds in their structure. Auxochromes act as a functional group for the molecule that can be hydroxyl (−OH), amino (−NH2), aldehyde (−CHO), methyl mercaptan (−SCH3) group, etc. Chromophores act as a part of the molecule and include unsaturated groups like methano (R_1-CH-R_2), azo (-N=N-), thio (-C=S), etc. They can be pH indicators, fabric dyes, azo groups, anthocyanins, and some metal chromophores like hemoglobin and chlorophyll.

1.6 Classification of dyes

Dyes can be classified based on their chemical structure, source, or application. Some of them are discussed here.

1.6.1 Direct dyes

Direct dyes are simple to use as they are directly applied to the fabrics in the form of a neutral or alkaline solution of dye. Direct dyes adhere to the substrate and form a hydrogen bond with it. These dyes are cheap compared to other dyes and give bright colors to fabrics. They fail to give good wash fastness. Direct dyes are mostly used to dye fabrics like cotton, paper, wool, silk, nylon, and other cellulosic fabrics. **Martius Yellow** is an example of direct dye. Its structure formula is given in Fig. 1.1[10].

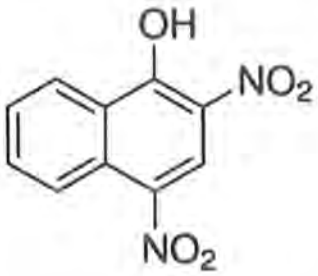

Figure 1.1: Structural formula of Martius Yellow.

1.6.2 Disperse dyes

Disperse dyes are not soluble in water and form colloids or dispersions. These colloids or dispersions get absorbed into the fabrics to color them. Dispersing agents can be used to finely grind and dissolve these dyes in the solution. Disperse dyes are used to dye cellulose acetate fibers, nylon, polyester, hydrophobic fabrics, and other nonionic synthetic materials[11]. **Disperse Yellow 3** and **Disperse Red 60** are examples of disperse dyes. Their Structural formula is given in Fig. 1.2[12].

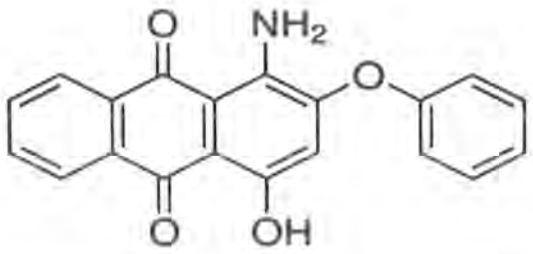

Figure 1.2: Structural formula of Disperse Red 60.

1.6.3 Reactive dyes

Reactive dyes have application in the form of a neutral or high pH solution, which is alkalized by other methods. They react by using nucleophilic substitution and nucleophilic addition methods. These dyes react directly with fiber due to the presence of a highly reactive chromophore attached to a substituent. They form a strong covalent bond when they are applied over a fiber. Due to this reason, these dyes show good fastness. These dyes can form a new chemical compound or give a new color to the fabrics after reacting with it. They give sharp colors that are durable and are not removed easily. Reactive dyes are used in the dyeing of cotton, polyamide, and wool. **Reactive Blue 5** dye is an example of reactive dye. Its structural formula is shown in Fig. 1.3[13].

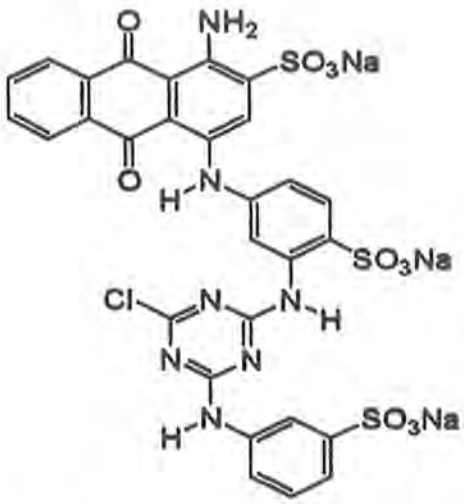

Figure 1.3: Structural formula of Reactive Blue 5.

1.6.4 Acidic dyes

Acidic dyes work in an acidic medium with a pH value of 2.6. They contain sulfonic (SO_3H) and carboxylic (COOH) groups. Due to the presence of SO_3H group, they have a negative charge and have an affinity for protein fibers. These dyes contain

an anionic part that helps dye become soluble in water and form an ionic bond with the fiber. Acidic dyes are used on wool, protein fibers, nylon, and silk. These dyes cannot be used for dyeing cotton. **Acid Red 138** is an example of an acidic dye and its structure is given in Fig. 1.4[14].

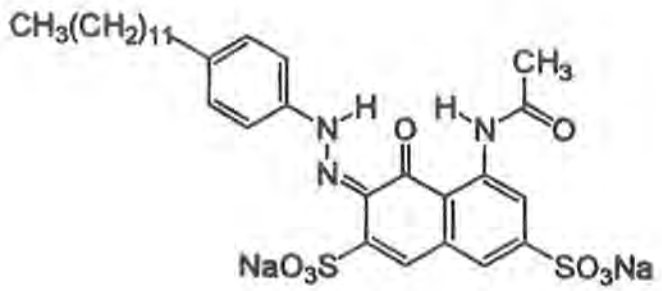

Figure 1.4: Structural formula of Acid Blue 138.

1.6.5 Basic dyes

Basic dyes are soluble in water, basic in nature, and contain a cationic part. This cationic component binds to the negative charge present in the fiber's structure. They contain auxochromes with basic functional groups such as amino groups, alkyl amino groups, $-NR_3$ or $=NR_2$. They give a bright color to the textile materials and are very economical. Basic dyes are used to dye wool, silk, and acrylic fibers. These are mostly used to give color to paper. **Basic Red 5** is an example of a basic dye whose structure is shown in Fig. 1.5[15].

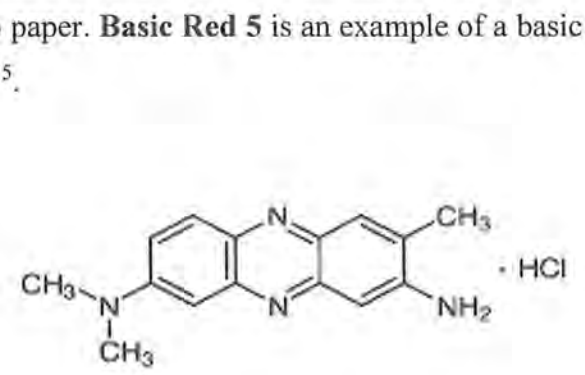

Figure 1.5: Structural formula of Basic Red 5.

1.7 Dyes as a water pollutant

Water pollution is mainly caused by effluents that are improperly released from industries without wastewater treatment. The textile industry plays a major role in polluting water as they use large amounts in dyeing, sizing, and washing[3]. These industries release many harmful chemicals, undesirable effluents, organic or inorganic solvents, toxic dyes, and heavy metals that have a high chemical oxygen demand. Most

of the dyes are not easy to degrade, are water insoluble, and are not easily removed by conventional methods. These factors leave an adverse effect on the marine life in waterbodies and the overall ecosystem.

Many ways are available to remove dyes from wastewater, among which physical, chemical, and biological methods are most effective. This selection depends on the type of contaminant present. All these methods have some advantages and disadvantages which are listed in Table 1.2[16]. In this way, the best ecofriendly and economical way of removing dyes in wastewater treatment is the photolysis of dyes.

Table 1.2: Methods for the removal of dyes.

Methods	Classification	Application	Disadvantages
Physical	Adsorption	Water soluble dyes	Form secondary dyes, poor adsorption
	Membrane filtration	Disperse dyes	Costly, consume metals like iron
Chemical	Electrochemical	Vat dyes, disperse dyes	Poor decolorization, not effective for cationic dyes
	Advanced oxygen	Acidic, basic, direct, reactive dyes	Poor removal of COD, high cost
Biological	Aerobic	Economical	Time consuming, unstable, dyes resistant
	Anaerobic	Removal colors easily	Carcinogens, toxicity

1.8 Photolysis/photocatalysis

By utilizing solar energy to degrade pollutants, photocatalysts enable the economically viable use of photocatalysis as a treatment method. Combining the words "photo" and "catalysis," we get "photocatalysis." Photons of light are referred to as photons, and catalysis is the process by which a catalytic substance modifies the activation energy barrier to change the reaction rate. By lowering the activation energy barrier without being spent, catalysts also speed up the reaction's completion. The same procedure is followed in photocatalysis where degradation occurs in the presence of sunlight. Main water pollutants that are treated by photocatalysis are listed in Table 1.3[17].

Table 1.3: Water pollutants treated by photocatalysis.

Pollutants	Examples
Cyanotoxins	Cyanobacteria, microtoxins
Pathogens	Bacterias like *Micrococcus lylae, E.coli, Hay bacillus*
CECs (Contaminants of Emerging Concern)	Dyes (methyl blue, methyl orange), Antibiotics, disinfectants, additives, Heavy metals (Cu^{+2}, Pb^{+2}, Cr^{+6}), Preservatives (salicylic acid)

Photocatalysis takes place in the following steps, light falls on the surface of a material (semiconductor) with high energy levels and initiates free radical mechanisms.

- Light falls on the semiconductor and electrons in valence band (VB) get excited and move to conduction band (CB).
- Catalytic semiconducting materials absorbed light from any illuminating source and created electron-hole pairs (e^-/h^+).
- Electron-hole pairs created oxidizing species such as superoxide ($.O_2^-$) and hydroxyl ($\cdot OH$) radicals that exhibit strong oxidation of organic materials.
- These free radicals attacked on contaminants where the reduction of CO_2 to CO occurs by electrons and oxidation of H_2O to O_2 occur by holes.

- Some other degradation byproducts were also formed.

The mechanism for photocatalytic degradation is given below in Fig. 1.6[18].

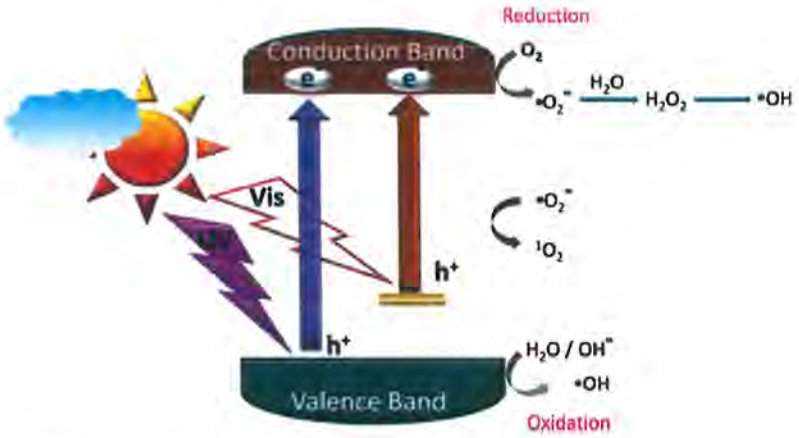

Figure 1.6: Mechanism of Photocatalysis.

1.9 Classification of photocatalysis

Based on the physical appearance of reactants, there are two types of photocatalysis.

1.9.1 Homogenous photocatalysis (photochemical)

In this type of photocatalysis, the photocatalysts and the reactants are in the same phase, like a solid, liquid, or gas. As indicated by the name "homo" which means same. It also involves the presence of a light absorber. This method is less expensive than other methods, such as the use of UV lamps or electrical sources[19]. For example, ozone and the photo-Fenton system (Fe^+ and Fe^+/H_2O_2).

1.9.2 Heterogenous photocatalysis

In this type of photocatalysis, the photocatalysts and the reactants are in different phases. They show a wide band gap and a narrow absorption range. Semiconductor materials do not have energy levels to allow the recreation of excitons. In these reactions, only photocatalysts are important and the photocatalytic activity mainly depends on the catalyst's ability to create excitons. In this method, a semiconducting material absorbs photons of light with an energy equal to or greater than the band gap of the material. Electrons move to the conduction band after excitation and form holes in the valence band. In order to increase the separation of electron-hole pairs, the exciton lifespan is extended using a variety of methods,

including substitutional doping and silver nanowires. In this way, excited electrons react with oxidants to form reduced products and holes form oxidized products. Redox reactions take place on the surface of semiconductors. For example, hydrogen transfer reactions, isotopic exchange reaction, etc[20].

1.10 Photocatalytic activity by Beer-Lamberts Law

The photocatalytic activity of the nanoparticles is checked using Beer-Lambert's Law[21]. This law shows the characteristics of the medium through which light is passing. In relation to UV-visible absorption spectrometry, the Beer-Lambert Law explains the absorption patterns, absorbance, and molar absorptivity of all light-active materials like solids, liquids, and gasses. The intensity of the light moving is calculated for each wavelength of light entering the spectrometer. The way light is absorbed by the sample in a cuvette is shown in Fig. 1.7.

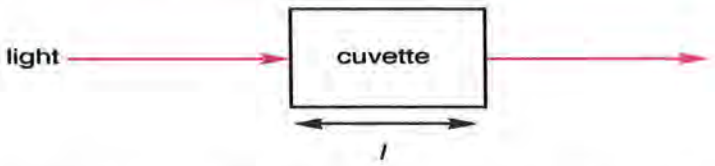

Figure 1.7: Light absorbed by sample in a cuvette.

This law demonstrates how a solution's absorption is inversely proportional to its concentration and to the width of the cuvette, which is the length of the light path.

$$A = \epsilon c l \quad \ldots\ldots (1)$$

Here,

A shows absorbance and has no units

ϵ shows molar absorptivity or molar extinction coefficient in $Lmol^{-1}cm^{-1}$ unit

c shows concentration of the solution measured in $molL^{-1}$ unit

l shows path length or width of cuvette measured in cm unit

This relation suggests that the absorbance of dye is directly related to its concentration. The percentage photocatalytic degradation efficiency (%PDE) of the sample can be estimated by using the relation in eq. 2.

$$\textbf{Degradation efficiency (\%)} = \frac{Co - Ct}{Co} \times 100 \quad \ldots\ldots (2)$$

Here,

Co shows initial concentration of dye before photo-irradiation and C_t shows concentration of dye after some time "t" of photo-irradiation. All this data is analyzed and collected with the help of UV-Visible spectrophotometry.

1.11 Choosing the best photocatalyst

The photocatalytic activity mainly depends on the band gap and electronic band structure of an appropriate semiconductor. Semiconducting materials with small band gap values show better photocatalytic activity. The band theory for states of matter shows that the band gap must be small. A low band gap value shows high absorption in the presence of visible light or natural sunlight. For productive use of the visible region of light, the band gap must range from **1.8–2.2 eV**. A good photocatalytic response is obtained at band gap energy (E_g) less than 3 eV[22].

In addition to the band gap effect, photocatalytic activity is also influenced by charge recombination. Charges in a semiconductor will try to recombine and form pairs, which will disturb the photocatalytic efficiency. So, this can be avoided by using the surface modification techniques, which will increase the separation of charges. One of the surface modification methods is the doping of any transition metal into a semiconducting metal oxide. In doping, impurities are added into pure substances and intrinsic semiconductors to change their properties. Semiconductors are not good conductors of electricity at low temperatures. But doping a semiconductor enhances its properties so it shows good conductivity even at low temperatures. A good photocatalyst must have these desirable properties

- Photoactive substance
- Good light absorption for better efficiency
- Photostability[23]
- High utilization of UV-Visible light
- Efficient and long lifetime charge separation
- Accessible and cost efficient

1.12 Mechanism of semiconductor photocatalysis

A photocatalytic reaction is initiated by using a light source such as UV light or sun. The photocatalysts absorb photons of light having energy more than their band gaps and form charge carriers (electrons and holes). Before the recombination of

photoinduced electrons and holes they diffuse to the surface of photocatalysts. They degrade the pollutants by redox reaction and form byproducts such as water and carbon dioxide[24]. Followed by valence band transition, electrons in the valence band move into the conduction band. Holes (h^+) and photoexcited electrons (e^-) will be produced in the valence band and conduction band, respectively.

Doped Mn_3O_4 will decrease the band gap and allow electrons and holes to react with O_2 and H_2O and form highly reactive superoxide anion radicals ($.O2^-$) and hydroxyl (.OH). The adsorbed O_2 over the photocatalyst capture e^- to form superoxide radical. It will react with water molecule to create hydroperoxy radical ($.HO_2$). Holes in valence band cause oxidation of adsorbed H_2O or OH^- to create hydroxyl radicals (.OH). Lastly, hydroxyl, hydroperoxyl, and superoxide radicals react with the dye and degrade it into organic pollutants i.e. CO_2, H_2O, and other minerals[25].

The general mechanism for the photocatalytic degradation of dyes by pure and doped Mn_3O_4 is as follows

$Mn_3O_4 + h\upsilon \rightarrow Mn_3O_4 (e^- \text{ and } h^+)$ ..... (3)

$O_2 + e^- \rightarrow .O_2^-$ ..... (4)

$.O_2^- + H_2O \rightarrow .HO_2$ ..... (5)

$h^+ + H_2O/OH^- \rightarrow .OH^-$ ..... (6)

$.HO_2/.O_2^-/.OH^-$ + dyes (MB, MO) → Degraded products ..... (7)

1.13 Photocatalysis in different materials

Photocatalysis can occur most efficiently in semiconductors. All the materials have a valence band and a conduction band. The band gap energy is the gap between these two bands. Photons of light provide energy for the electron's excitation. An electron residing in the valence band requires more energy to be excited if the band gap between the conduction and valence bands is wide. It can occur with the availability of light of a suitable wavelength for conduction. This suitable wavelength can be calculated by the following mathematical relationship.

$$\frac{1240}{Eg} = \lambda \quad \text{..... (8)}$$

The photocatalytic effect mainly depends on the band gap or energy gap between VC and CB. Band gap energies for conductors, insulators, and semiconductors

are different. The band gap value for an insulating material is very high, at +5 eV. So, very high energy photons are required for the excitation of electrons. The conducting materials (metals) have no energy band gap, and the value is >0.1 eV. They rely on the band position[26]. Semiconductors have an occupied valence band and an unfilled conduction band. Semiconductors have a higher band gap energy than conductors but a lower band gap energy than insulators that is approximately 1 eV. It concludes that semiconducting materials are the best selection for photocatalysis. The band gaps for different materials is shows in the Fig. 1.8[27].

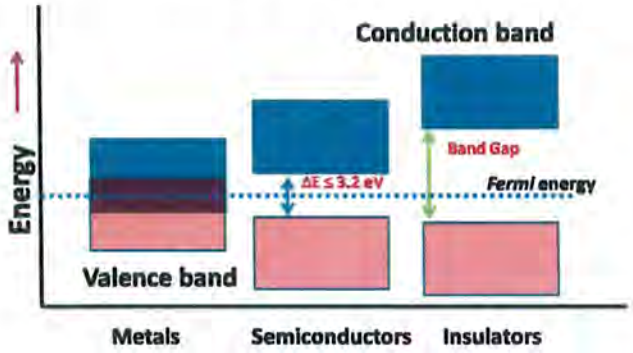

Figure 1.8: Band gaps of (a) metals (b) semiconductors (c) insulators.

1.14 Overview of synthesized NPs and dye used in photocatalytic degradation

Different materials show different catalytic activity with various dyes. In our research work, we have synthesized pure and Nickle (Ni) doped Mn_3O_4 nanoparticles (NPs). Dyes used were Methyl blue (MB) and Methyl orange (MeO).

1.14.1 Introduction to Mn_3O_4 NPs

Manganese oxide is a p-type semiconducting metal oxide with a band gap energy of 2.5 eV. It is brownish black colored powder at room temperature. Its mineral name is hausmannite and its molecular density is 4.84 gcm^{-3}. Mn_3O_4 nanoparticles have a wide band gap which makes it highly conductive and restrict the recombination of electrons and holes. They show high thermodynamic properties with many chemical and physical properties. These nanoparticles have a distorted spinel structure with tetragonal and orthorhombic phases. They show two oxidation states i.e. Mn^{+2} and Mn^{+3}. Tetragonal phase of Mn_3O_4 exist at steady room temperature in which Mn^{+2} ions are present in tetrahedral position while Mn^{+3} ions are present in octahedral position[28].

The nanostructured Mn_3O_4 has a wide range of application in different fields, including the production of water purification systems, biosensors, energy devices, and reaction catalysts. These nanomaterials can be used as an advanced antibacterial agent to reduce the number of drug-resistant microbes in the environment. They have high oxidation potential and show good oxidative ability. These nanoparticles have enhanced photocatalytic activity due to its band gap and spinel structure[29]. Synthesis Mn_3O_4 can occur through various methods and techniques like hydrothermal[30], solvothermal[31], reflux method[32], precipitation method[33], sonochemical method[34], or by solution combustion method[35]. Each of these methods will result in formation of nanoparticles with alternative electrical and optical properties. Crystal structure of Mn_3O_4 is shown in Fig. 1.9[36].

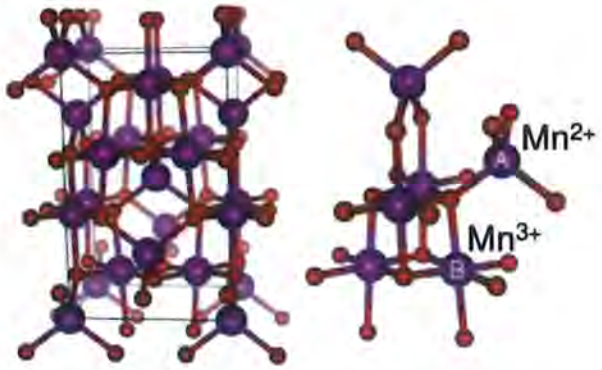

Figure 1.9: Manganese Oxide spinel structure.

1.14.2 Introduction to Methyl blue dye (MB)

Methyl blue is a cationic and basic dye in nature[37]. Its molecular formula is $C_{37}H_{27}N_3Na_2O_9S_3$. It is present in the form of blue crystals and give rich blue color when dissolved in water. The structure of MB dye is shown in the Fig. 1.10[38].

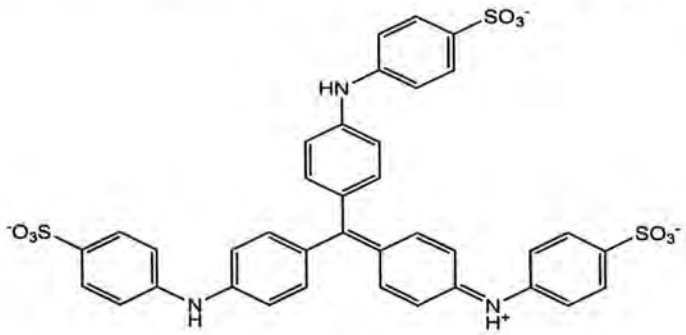

Figure 1.10: Structural formula of Methyl blue dye.

It is a plasma stain and is used for cytology and staining of histological sections. It is also used as an indicator and in dyeing cotton and silk. Methyl blue dye has reached a safer choice criteria but it can cause some hazardous issues too. It can create eye infections, respiratory issues like asthma, and skin allergies. The measured maximum absorption peak of methyl blue is at 664 nm wavelength. It is shown in Fig. 1.11.

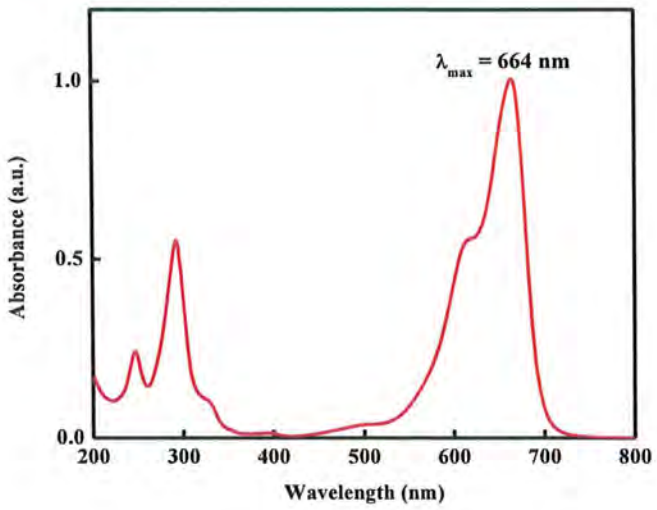

Figure 1.11: Absorption spectra of Methyl blue dye.

Figure 1.12: Methyl blue dye solutions.

1.14.3 Introduction to Methyl orange dye (MeO)

Methyl orange dye is an anionic dye with $C_{14}H_{14}N_3NaO_3S$ molecular formula. It appears as orange colored powder and its solution appears orange in color as sown in Fig. 1.15. When methyl orange is dissolved in water, it is transformed from a weak acid into neutral orange molecules. Structure of MeO dye is shown in the Fig. 1.13[39].

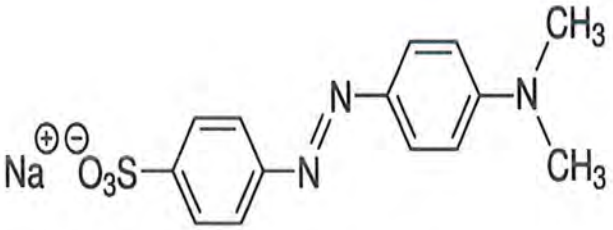

Figure 1.13: Structure of Methyl orange dye.

MeO dye is an azo dye and it exhibits at various pH levels. The colour of the solution changes from yellow to red when methyl orange is employed as an acid indicator. When it is used as a basic indicator, the solution becomes yellow in color[40]. It is a highly colored chemical and is mostly used in printing and dyeing. On the other hand, MeO dye is hazardous and can be carcinogenic. The measured absorption peak of MeO dye appears at 465 nm wavelength as shown in Fig. 1.14.

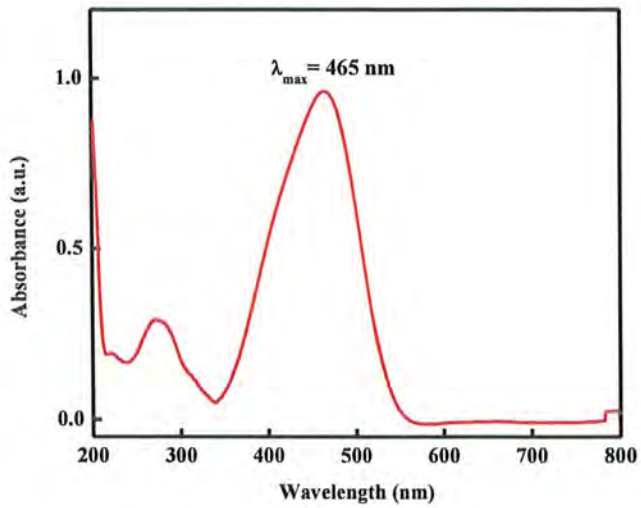

Figure 1.14: Absorption spectra of Methyl Orange dye.

Figure 1.15: Methyl Orange dye solutions.

1.15 Kinetic study of semiconductor photocatalytic activity

In a photocatalytic reaction, the rate depends on the concentration of electrons and holes generated by photoexcitation. The concentration of photogenerated electrons and holes depends on the recombination of charges and the intensity of light. The steady-state approximation (SSA) suggests the highest achievable concentration of excitons (electron-hole pairs). SSA mainly depends on the electronic and structural characteristics of semiconductors. It may also be affected by the presence of any additive in the reaction mixture. Temperature and pressure can also disturb the SSA.

1.15.1 Langmuir–Hinshelwood kinetic model of photocatalysis

For the estimation of photocatalytic activity, temperature rate constant is determined. Photocatalysis is a pseudo first order reaction. A number of organic dye molecules have undergone photocatalytic degradation, and the kinetics of this process have been described using the Langmuir-Hinshelwood equation[41]. The reaction rate in this model is predicated on how much of the photocatalyst's surface is covered by the material[42].

$$r = -\frac{dC}{dt} = k\theta \quad \ldots\ldots (9)$$

Where k is the rate constant of reaction kinetics.

$$\theta = \frac{Kc}{(1+Kc)} \quad \ldots\ldots (10)$$

Where K is the constant of the reactant adsorbed on the surface of semiconducting material.

The L-H model describes the photocatalytic degradation of dyes when the contaminant is adsorbed on the surface of the catalyst since it depends on the degree of adsorbed pollutant on the photocatalytic surface. Substituting eq. 10 in eq. 9 and we get

$$r = k\frac{Kc}{(1+Kc)} \quad \ldots\ldots (11)$$

Integrating this eq between 0-1 limit will give

$$ln\frac{Co}{C} + K(Co - C) = kKt \quad \ldots\ldots (12)$$

Where

t is the time of irradiation.

Co is the concentration of substance before photoirradiation

C is the concentration of substance at any time t after photoirradiation

The half-life for a first order reaction is calculated by this formula.

$$t_{1/2} = \frac{0.963}{k} \quad \text{..... (13)}$$

$t_{1/2}$ is the reaction's half-life with seconds (s) as a unit and k is the reaction's rate constant with $M^{(1-n)}s^{-1}$ as a unit where n is the order of reaction.

Literature review:

S. Karpagavalli et al.,[43] investigated the optical and electrochemical characteristics of Ni-doped Mn_3O_4 semiconductors with the effect of doping on the magnetic properties of synthesized materials by solvothermal method.

Larbi T. et al.,[44] reviewed the photocatalytic activity by using hausmannite (Mn_3O_4) nanoparticle along with their synthesis, phase transformation, and morphology. They confirmed the tetragonal structure of Mn_3O_4. Their studies revealed that the dependence photocatalytic activity on band gap.

Brites F. et al.,[45] explained about the dependence of degradation of dyes on concentration and treating the kinetic data in terms of pseudo-first order rate. It tells photocatalytic activity of dilute solutions is easy.

Raja G. et al.,[46] synthesize Mn_3O_4 nanomaterials by microwave technique and explained the effect of Nickel doping on the property of electrochemical water oxidation of Mn_3O_4 nanomaterials. This reading shows the relationship of atomic radius of Ni and Mn on the size of crystals formed.

Sahoo C. et al.,[47] investigated the ability of Ag^+ doped TiO_2 NPs for the photocatalytic degradation of Methyl blue dye. This study explains the impact of concentration, pH and catalyst on the MB degradation. The dye decolorization and mineralization percentages under ideal conditions were anticipated to be 95.97% and 80.33 percent, respectively.

Jamali-Sheini, Farid et al.,[48] used stannous sulfide (SnS) NPs synthesized by sonochemical method, to check the photocatalytic degradation of Methyl blue dye.

Size, defects/impurities, band gap, and photocatalytic effectiveness were all significantly influenced by the sonication frequency.

Jose Colina–Márquez et al.,[49] analyze that several industrially used dyes and pigments for their ability to degrade using the kinetic and adsorption properties of TiO_2-based nanomaterials. He examined that heterogeneous photocatalysis was used as a treatment.

Tawfik A. Saleh et al.,[39] showed that the hazardous dye methyl orange is degraded through photocatalysis using a composite catalyst made of carbon nanotubes and titanium dioxide.

Hongzhu Ma et al.,[50] study the use of the combined electrochemical technique for degrading wastewater containing methyl orange and the effect of degradation on the UV-Visible spectrum. It showed 100 % disappearance of color.

Lili Kuang et al.,[51] explained the electronic and magneto-optical properties of Mn_3O_4 NPs and effect of doping on tuning the energy band gap.

Aims and Objectives

When resources are no longer usable, the world in which we currently live will end one day. To satisfy needs and desires, humans have created a variety of dangerous compounds that are inadvertently contaminating our surroundings. Life on earth mainly depends on water in to survive. Textile industries produce waste and hazardous chemicals like dyes, which drain into the water without any adequate treatment. The content of minerals and nutrients in the water has been impacted by these effluents. There is a lack of wastewater treatment resources that can effectively remove these pollutants.

The most efficient chemical approach for dye breakdown is the photocatalytic reaction. To accelerate the decoloring of dye, we employed nanoparticles of Mn_3O_4 doped with transition metal (Ni). Mn_3O_4 NPs are environment-friendly and non-toxic. It is safe in usage and gives good results for the degradation of MB and MeO dye. We have also put a lot of effort into protecting the environment by taking the initiative to efficiently control and decrease debris to far less harmful materials. Water is an essential element of our environment. Our efforts would help to maintain a clean environment, which in turn would help the earth's ability to support life for an extended period.

CHAPTER 2: MATERIALS AND METHODS

2.1 Chemicals that are used

For the synthesis of pure and doped Mn_3O_4 nanoparticles, the chemicals were taken from Sigma Aldrich supplier. I have used Manganese dichloride tetrahydrate ($MnCl_2.4H_2O$) as a precursor or salt. It is available in pink solid powdered form and has 99% percentage purity. I used Sodium hydroxide (NaOH) to initiate the formation of manganese oxide nanoparticles. NaOH is anhydrous and freshly prepared solutions were used. It has percentage purity of 99%. CTAB ($C_{19}H_{42}BrN$) was used as a surfactant. It is available in a white powdered form. Nickel acetate ($Ni(CH_3CO_2)^2$) was taken as a dopant. It is available in the form of powder which are green crystals in color. Methanol (CH_3OH) and deionized water were used for the washing of materials. The photocatalytic activity of materials were checked by using Methyl Blue dye ($C_{37}H_{27}N_3Na_2O_9S_3$) that is blue in color and Methyl Orange dye ($C_{14}H_{14}N_3NaO_3S$) that is orange in color.

2.2 Synthesis

2.2.1 Procedure for the synthesis of pristine manganese oxide NPs.

For the synthesis of pure manganese oxide nanoparticles, co-precipitation method was used. In a two neck round bottom flask, 2.17 g of $MnCl_2.4H_2O$ was dissolved in 100 mL of deionized water. NaOH solution was prepared by dissolving 0.88 g of NaOH in 100 mL of deionized water under constant stirring till sodium hydroxide was dissolved. Then added NaOH solution into the $MnCl_2.4H_2O$ solution dropwise, with continuous stirring. Brown color precipitates began to form gradually and the solution become brown in color. 0.025 g of CTAB solution was prepared in 50 mL of deionized water and then it was added into the main solution. It was stirred at room temperature for 24 hours under constant magnetic stirring at moderate speed.

The obtained precipitates were filtered and then washed with deionized water and methanol for several times. Dried the sample in oven at 80 °C for 12 hours. The sample was grinded and calcined at 350 °C for 2 hours. Brownish black colored Mn_3O_4 nanoparticles were obtained.

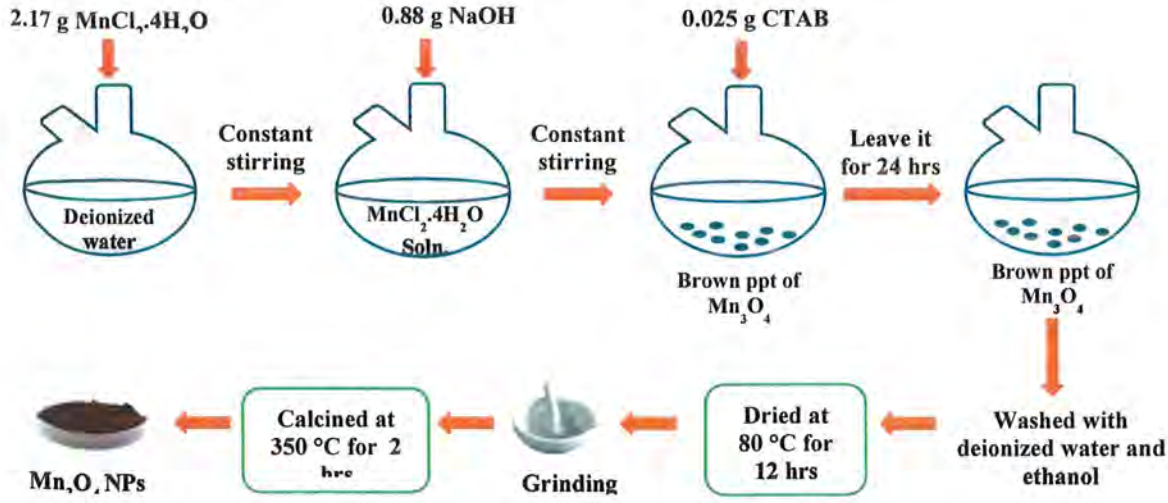

Figure 2.1: Flow sheet diagram for synthesis of Mn_3O_4 NPs.

2.2.2 Procedure for the synthesis of Nickel doped manganese oxide NPs.

For the synthesis of nickel doped manganese oxide nanoparticles, first of all added weight (1-4) % of nickel acetate in deionized water and stirrer to get a homogenous solution. Color of solution was changed from transparent. After that solution of 2.17 g of $MnCl_2.4H_2O$ was added in it. 0.88 g of sodium hydroxide solution was added into it dropwise. 0.025 g of CTAB solution was prepared in 50 mL of deionized water and then it was added into the main solution. Repeated the same process that is written above. It resulted in the formation of (1-4) % composition of Nickel doped manganese oxide nanoparticles of different percentages.

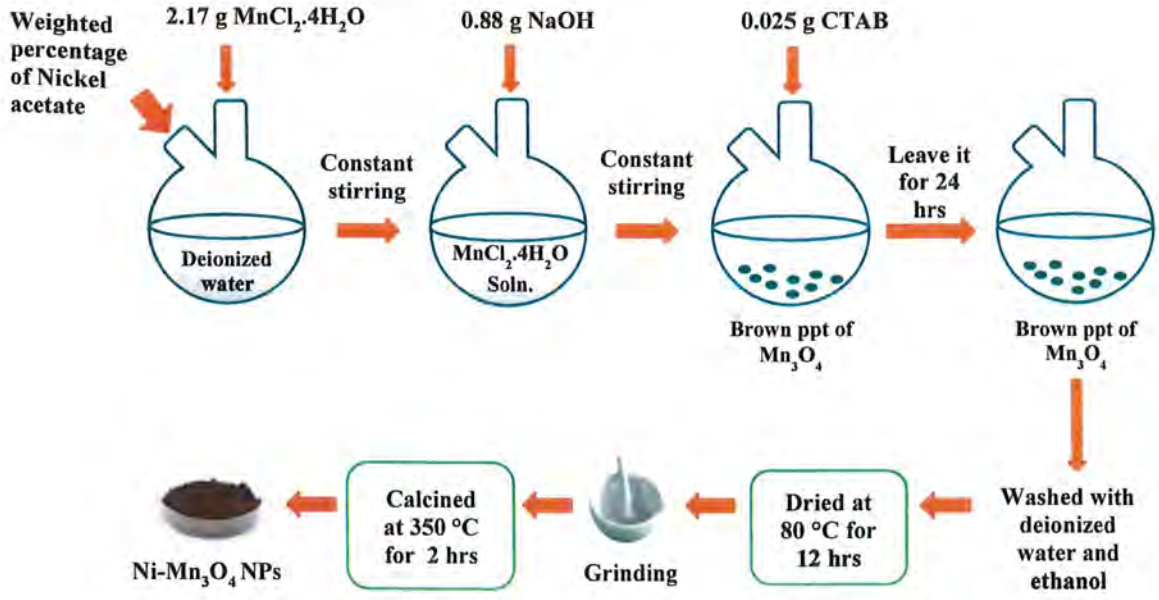

Figure 2.2: Flow sheet diagram for synthesis of (1-4) % Ni-doped Mn_3O_4 NPs.

2.3 Experimental setup for the absorbance measurement of dyes

For the purpose of determining the photocatalytic activity of pure and Ni-doped Mn_3O_4, the photodegradation of MB and MeO dye was investigated in deionized water solution. Photodegradation of dyes was taken in September October 2022. Dyes show degradation in the presence of prepared photocatalysts. Stock solution of both dyes were prepared for photocatalysis. First of all 1 mM stock solution of pure MB dye was prepared by dissolving 0.0095 g of dye in 30 mL of deionized water. Then 30 μM solution was prepared from the stock solution in 25 mL deionized water. In order to reach adsorption and desorption equilibrium, 2 mg of catalyst was added to the produced dye solution and kept on stirring in the dark for 30 minutes. After this time, a very minute amount of the aliquot was obtained. The absorbance of this sample was determined through UV-Visible spectrophotometry which gave initial reading as A_o. The sample was placed in sunlight and is exposed to irradiation for two hours and 30 minutes with constant stirring with a magnetic stirrer. UV absorbance was measured from a spectrophotometer after every 15 minute and these values were recorded as A_t. For MeO dye, 0.0098 g of dye was added in 30 mL deionized water to form 1 mM stock solution. Then followed the same procedure discussed above. The general scheme for the absorption study of dye degradation is shown in Fig. 2.3.

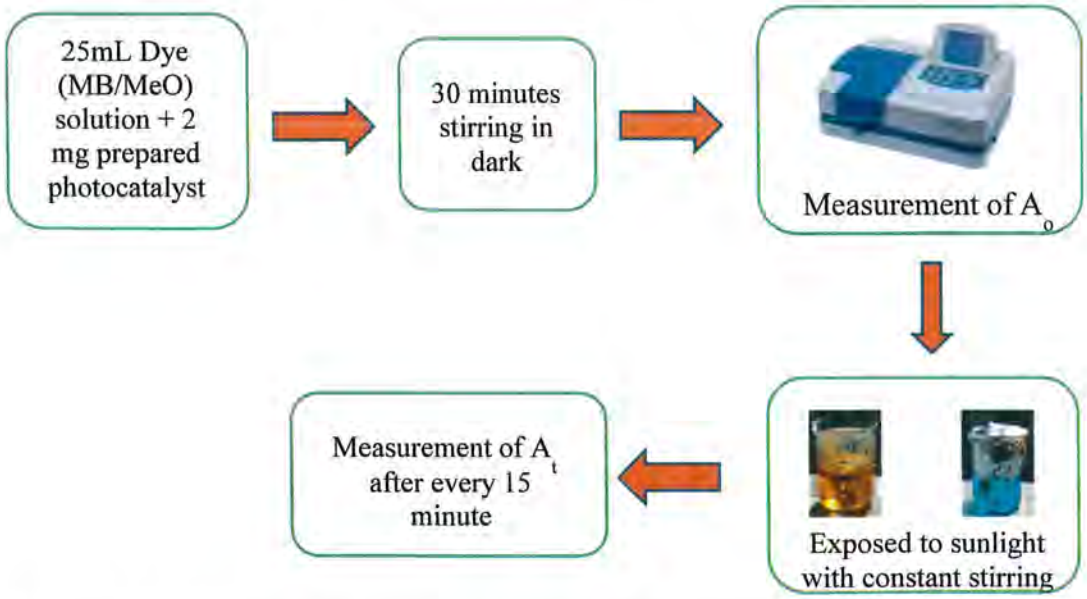

Figure 2.3: Flow sheet diagram for the photocatalytic studies of MB and MeO dye.

After analyzing the photocatalytic activity of synthesized NPs, four different parameters were assessed to find optimal conditions for dyes. These parameters were effect of concentration of dopant, amount of catalyst, concentration of dye, and pH.

Effect of concentration of dopant

In this study, 2 mg of pure and (1-4) % Ni-doped Mn_3O_4 NPs were added to five beakers having 25 mL of stock solution for both dyes separately. Then the above discussed protocol was followed. In first step, 4 % Ni-doped Mn_3O_4 NPs gave the maximum photodegradation efficiency for MB dye while 2% Ni-doped Mn_3O_4 NPs gave the maximum photodegradation efficiency for MeO dye.

Effect of amount of catalyst

Dose of catalyst ranging from 1 to 4 mg of the optimized catalyst were used. 1, 3, and 4 mg of the selected photocatalyst were added to a 25 mL stock solution of dye in three separate beakers. 3 mg of 4 % Ni-doped Mn_3O_4 NPs gave the best photocatalytic degradation efficiency for MB dye, and 2 mg of 2 % Ni-doped Mn_3O_4 NPs gave the best photocatalytic degradation efficiency for MeO dye.

Effect of concentration of dye

The dye concentration was observed by making different concentration of dye solution ranging from 25 μM to 35 μM for MB dye and 70 μM to 90 μM for MeO dye. The concentrations were made by using optimized amount of catalyst of 3 mg of 4 % Ni-doped Mn_3O_4 NPs for both concentrations of MB dye and 2 mg of 2 % Ni-doped Mn_3O_4 NPs for MeO dye.

Effect of pH

The pH was studied at five different pH values ranging from 1 to 11 while the solutions used earlier were at pH 7. Firstly, 25 mL of optimized concentration of dye solutions were made from the stock solution of both dyes in separate beakers. The pH was maintained in the dye solution by using HCl for acidic and NaOH for basic pH. Then 3 mg of 4 % Ni-doped Mn_3O_4 NPs were added for MB dye and 2 mg of 2 % Ni-doped Mn_3O_4 NPs were added for MeO dye respectively. Then they were exposed to sunlight with constant stirring. Maximum %PDE came at pH 11 for MB dye after 75 minutes and at pH 5 for MeO dye after 90 minutes.

2.4 The source of light

Direct sunlight was used as a light source for the photocatalytic degradation of organic dyes. The range of wavelength is 200 to 800 nm.

2.5 Analysis

The degradation of dyes in the presence of photocatalyst was monitored and recorded by using UV-Visible spectrophotometer. MB dye started degrading at 664 nm of wavelength and MeO at 465 nm of wavelength respectively.

2.6 Kinetic analysis

Four steps were performed to completely study the photodegradation kinetic measurements. For the kinetic analysis of dyes, solutions were prepared in de-ionized water. Dye solutions with catalyst were in sunlight in every step for the degradation of dye. First of all, percentage of dopant was changed while all the other factors were constant which includes amount of catalyst, dye concentration, and pH. In the same way, all factors were studied one by one by keeping other constant. Initial reading was taken as A_0 while the other readings were recorded after every 15 minute as A_t. The plot of ln (A_0/ A_t) vs time was used to determine the rate of reaction.

2.7 Characterization techniques

2.7.1 UV-Visible Spectroscopy

UV-Visible spectrophotometer was used to see the spectrum and optical properties of compounds formed. It was also used to analyze the degradation of dyes used i.e., MB and MeO. The idea behind a UV-Visible spectrophotometer is that different materials absorb ultraviolet or visible light in different ways, each of which results in a distinct spectrum. A material absorbs light through excitation and de-excitation in spectroscopy. A spectrum is created as a result of this interaction between light and matter. Schematic representation of UV-Visible spectrophotometer is shown in Fig. 2.4[52]. When UV light passes through the solution containing material under investigation, the electrons in the matter which are in low energy state gets energy from light and jump to their higher energy states. This is based on Beer's lambert law which implies that concentration and absorption are directly proportional to each other[21]. It is represented mathematically by this relation.

$$A = \varepsilon bc.$$

Where A is a unit less quantity that denotes absorbance. The molecular absorptivity coefficient is ε having $Lmol^{-1}cm^{-1}$ unit, b is the optical path length of cuvette that is 1 cm and c shows the solution's concentration in $molL^{-1}$ unit. So this technique was used to determine the UV-Visible spectra and band gaps of pure and doped Mn_3O_4 NPs. Tauc plots were used to calculate the band gaps.

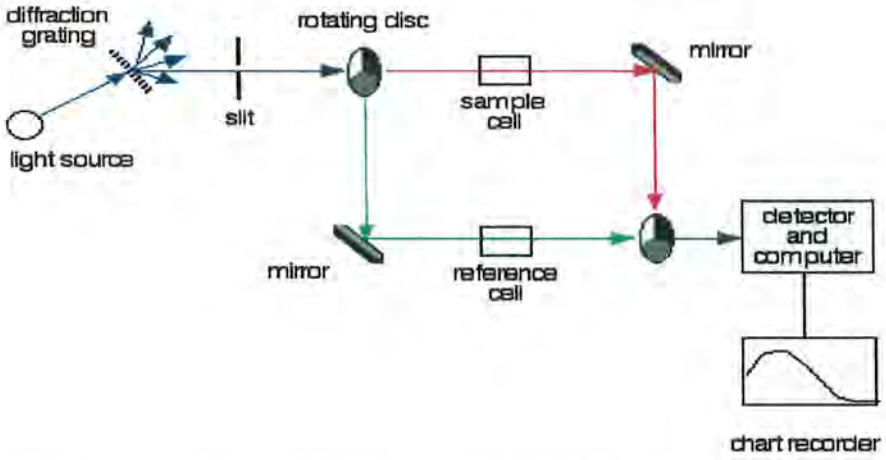

Figure 2.4: Schematic representation of UV-Visible spectrophotometer.

2.7.2 X-Ray Diffraction (XRD)

It is a non-destructive laboratory method that analyses the lattice spacing of crystalline substances in the form of powder, thin films, and bulk. Lattice spacing and distortions can be used to identify unidentified materials, residual stresses, and elastic properties in a sample. By beaming an X-ray into the synthesized crystalline material at a known wavelength λ, and a known angle θ, XRD gets lattice spacing and measures the intensity of the refracted X-rays. Schematic diagram of Powder X-Ray Diffraction is shown in Fig. 2.5[54].

The powdered XRD technique will give intensity readings for the sample. Multiple intensity readings will appear if the sample has more than one material in the sample[53]. XRD is time efficient and is frequently economical as well.

0.2 mg of the synthesized sample was used to compare pure and Ni-doped Mn_3O_4 NPs. Cu-k radiation (λ =0.154 nm) was employed in the X-ray Diffraction Bruker AXS B8 Discover mode, and graphite served as a monochromator. The samples were tested across a 2 range between 200 and 800 nm. Debye Scherer equation was used to determine the crystallite size of pure and Ni-doped Mn_3O_4 NPs.

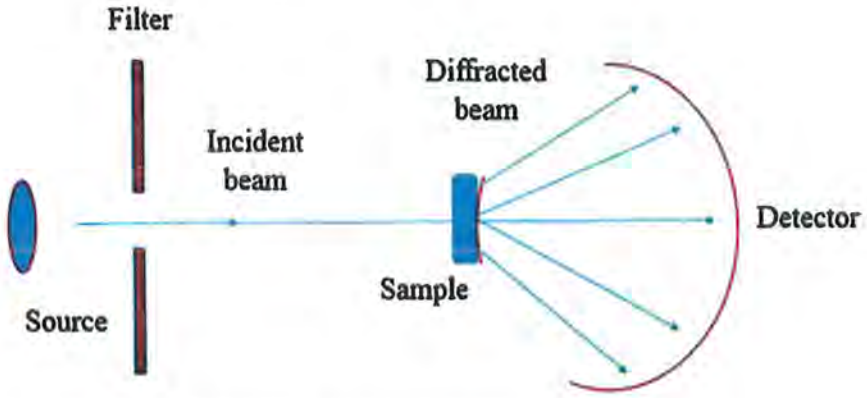

Figure 2.5: Schematic representation of XRD analysis.

2.7.3 Fourier transform infrared spectroscopy (FT-IR)

The data from an interferometer with a moving mirror is Fourier transformed to get an IR spectrum, which is then used by FT-IR spectrometers to create an optical transform of the infrared signal. Fourier analysis will give an IR spectrum that is the relationship between intensity and frequency. Gases, liquids, and solids can all be easily and quickly analyzed using the FT-IR method[55].

It provides information about various vibrational bands of the elements present in the sample. For any specific molecule, the pattern of vibrations is distinct. Each group vibrates in a variety of ways in the IR region, including stretching, bending, rocking, and other motions. The nature of sample for qualitative analysis is directly indicated by the peak intensity. It tells about the presence of organic and inorganic compounds. Different functional groups can also be detected by FT-IR analysis as shown in Fig. 2.6[56].

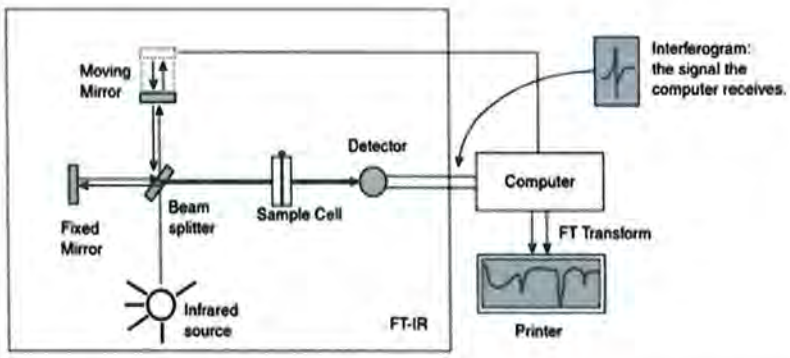

Figure 2.6: Schematic representation of FT-IR spectrophotometer.

Chapter 3: RESULTS AND DISCUSSION

3.1 UV-Visible Spectroscopy:

The UV-Visible spectroscopic analysis was done in the wavelength range of 200 to 800 nm. The samples were prepared by using deionized water as a solvent. Absorption spectrum data helped in the estimation of band gaps of samples by using tauc plots. The material's optical band gap energy can be obtained by extrapolating the linear portion of the absorption curve[43]. The UV-Visible absorption spectrum of pristine and Ni-doped Mn_3O_4 nanoparticles is shown in Fig. 3.1.

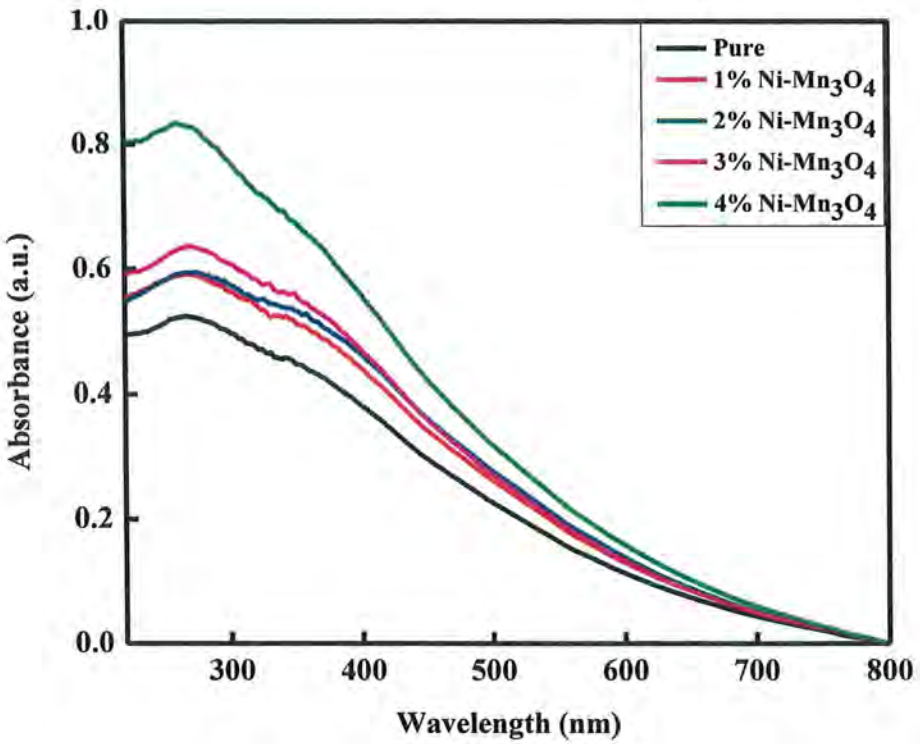

Figure 3.1: UV-Visible absorption spectrums of pure and (1-4) % Ni-Mn_3O_4 NPs.

Pure and Ni-doped Mn_3O_4 nanoparticles possess strong absorption peaks in the range of (250-410) nm. The absorption spectrum of pure Mn_3O_4 nanoparticles showed a maximum absorption wavelength peak (λ_{max}) at 266 nm[57]. Band gap of pure Mn_3O_4 NPs was obtained by tauc plot that is 2.50 eV as shown in Fig. 3.2 and Fig 3.3.

3.1.1 UV-Visible spectrum of Ni-doped Mn_3O_4 nanoparticles:

1 % nickel doped Mn_3O_4 NPs shows the maximum absorption peak at 270 nm and the band gap is at 2.46 eV. Fig. 3.3 shows the bandgap which confirmed a slight red shift in the absorption peaks that cause narrowing of energy band gap. The maximum absorption peaks for the (2-3) % Ni- Mn_3O_4 were at 273 nm, 285 nm respectively. The band gap values for these samples were at 2.41 eV to 2.37 eV respectively. This shows an increase in wavelength which resulted in the decrease in the band gap energy known as red shift. This occurs due to new energy levels created by Ni due to charge transfer between dopant and material so the band gap falls[58]. Illustrated according to this relation

$$\mathbf{E = hc/\lambda}$$

The absorption spectra for the 4 % Ni-Mn_3O_4 NPs shows maximum absorption peak at 260 nm. It shows a reduction in wavelength which indicates blue shift or bathochromic shift and as a result there is an increase in band gap energy that is 2.54 eV. This occurs due to quantum size confinement that decreases the particle size and as a result deformation of the Mn_3O_4 lattice structure takes place. This is also explained by the Burstein Moss effect according to which after a certain concentration of dopant, all the fermi levels in conduction band were occupied so excited electron move to the conduction band above the fermi levels and as a result there is an increase in band gap[59]. The values of maximum absorption peaks and their respective band gaps of the nickel doped Mn_3O_4 NPs are given in Table 3.1.

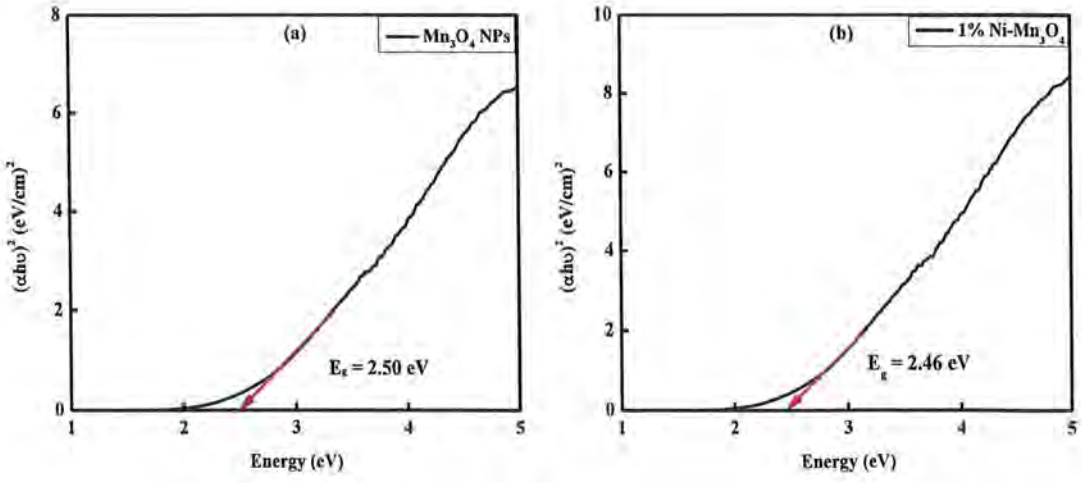

Figure 3.2: Band gaps of Mn_3O_4 and 1 % Ni-Mn_3O_4 NPs.

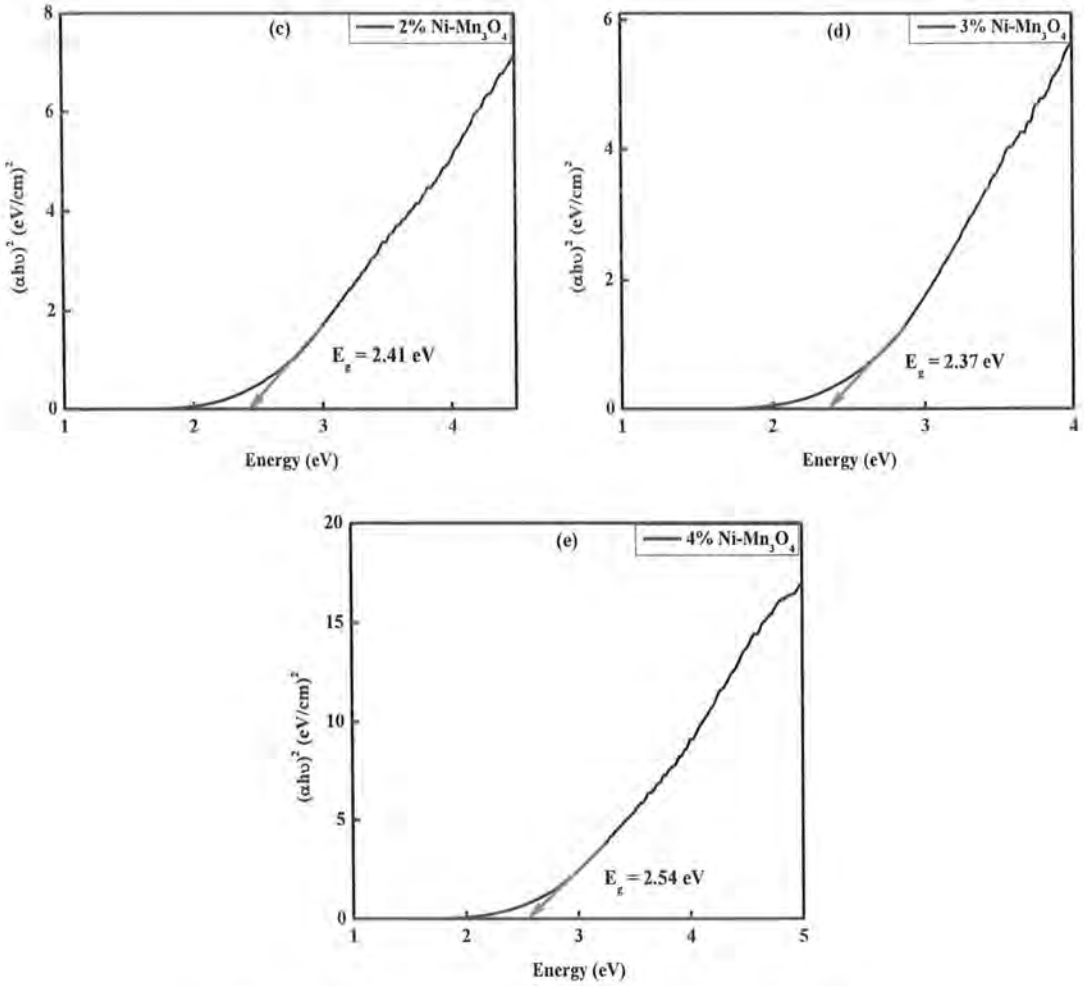

Figure 3.3: Band gaps of (2-4) % Ni-Mn_3O_4 NPs.

Table 3.1: Band gaps and max. absorption peaks of pure and (1-4) % Ni-Mn_3O_4 NPs.

Sr. No.	Sample	Maximum Absorption Peak (nm)	Band gap (eV)
1	Mn_3O_4	266	2.50
2	1% Ni-Mn_3O_4	270	2.46
3	2% Ni-Mn_3O_4	273	2.41
4	3% Ni-Mn_3O_4	285	2.37
5	4% Ni-Mn_3O_4	260	2.54

3.2 X-Ray Diffraction (XRD)

The XRD pattern of pure Mn_3O_4 nanoparticles is shown in the Figure 3.3. The crystallographic planes (112), (103), (211), (220), (321) and (224) corresponds to the detected diffraction peaks at 2θ values of 28.967°, 32.533°, 36.191°, 44.600°, 58.765°, and 60.026°, respectively. The diffraction peaks confirms the formation of Mn_3O_4 single phase[46]. The sharp and broad peaks of the Mn_3O_4 were may be a result of the crystalline structure of pristine Mn_3O_4 shown in Fig 3.4. These peaks supported the tetragonal structure of manganese oxide and satisfactorily met the Joint Committee on Powder Diffraction Standards (JCPDS) requirements (reference file no. 00-001-1127)

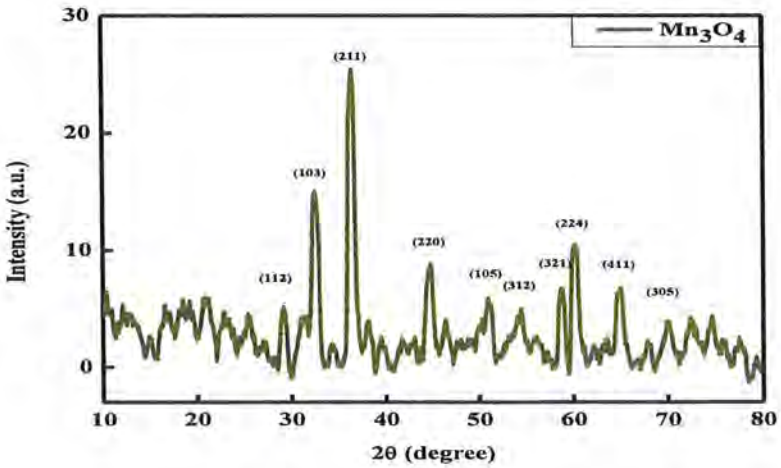

Figure 3.4: XRD spectrum of pure Mn_3O_4 NPs.

XRD patterns of pristine Mn_3O_4 and Ni doped Mn_3O_4 NPs as shown in Figure 3.5. No impurity peaks or nickel related phases were found after nickel doping of Mn_3O_4 NPs. Additionally, it was observed that when the concentration of Ni rises, the most intense peak gradually widened and shifted to a higher angle. This confirmed that Ni and Mn ions are equally dispersed and Ni ions have replaced Mn ions in the Mn_3O_4 tetragonal structure without any distortion. According to Bragg's equation,

$$n\lambda = 2d\sin\theta$$

This equation shows inverse relation between d-spacing (d) and diffraction angle (θ). Widening of peaks and shifting towards higher 2θ values is because of decrease in d-spacing between planes. This occurs due to difference in ionic radius of

Ni and Mn ions. As the ionic radius of Ni is less than Mn, so it cause a decrease in d-spacing which will shift the peak values to a higher angel[60].

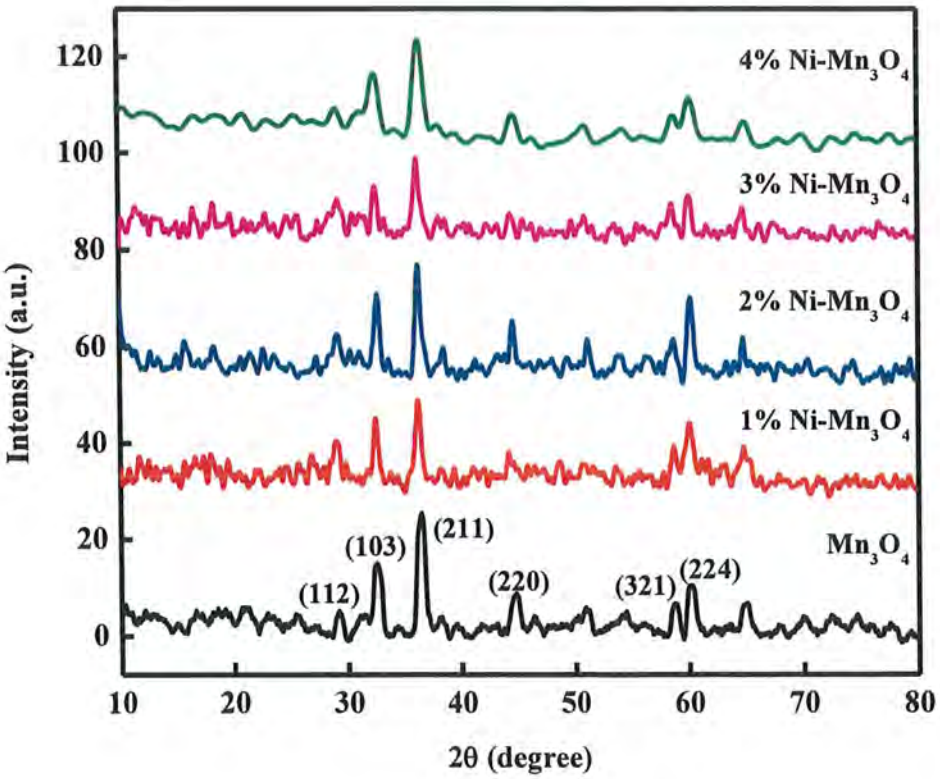

Figure 3.5: XRD patterns of pure and (1-4) % Ni-Mn_3O_4 NPs.

The crystallite size of prepared samples can be calculated by using Debye Scherrer expression.

$$D = \frac{0.9\lambda}{\beta\cos\theta}$$

Where,

D= Average crystallite size (nm)

λ= X-Ray source wavelength (1.5404 Å)

β= Full widths-at-half-Maximum (FWHM) of peaks in radians

θ= Bragg's diffraction angle (degree)

Table 3.2: Crystallite sizes of pure and (1-4) % Ni-Mn_3O_4 NPs.

Sr. No.	Samples	Crystallite size (nm)
1	Mn_3O_4	12.14
2	1% Ni-Mn_3O_4	14.16
3	2% Ni-Mn_3O_4	14.26
4	3% Ni-Mn_3O_4	14.59
5	4% Ni-Mn_3O_4	11.56

Table 3.2 shows the crystallite size of pure and Ni-doped Mn_3O_4 NPs. It shows that the crystallite size, unit cell volume, and lattice constant increase with doping. At the boundary of Ni doped Mn_3O_4 grains, inversion boundaries were created and the crystal grow in a path parallel to the plane of an inverted boundary. The crystallite size increase with increasing dopant concentration up to 3% Ni-Mn_3O_4 NPs. After that, increase in Ni concentration will cause a decrease in crystallite size which might be due the oxygen desorption or settlement of Ni within the lattice structure which form bonds with unstable oxygen atoms of Mn_3O_4. Interfacial grain formation is also hindered by formation of multiple channels of Ni ions at surface of Mn_3O_4[61].

When the concentration of dopant increase it affects Mn site symmetry. Mn^{+3} ions occupy octahedral sites in spinel structure and have no orbital angular momentum. Ni substitutions exchange coupling in this mixed spinal system[46]. So, valency of Mn ions change from trivalent to divalent and thus Mn ions move to tetrahedral site while Ni substitute in octahedral site keeping normal spinel structure. This suggests that Ni doping affect the size of the particles. This variation is brought about by the strain, crystallite size, and lattice characteristics which lead to a higher broadening of diffraction peak.

3.3 Fourier Transform Infrared Microscopy (FT-IR)

Significant qualitative information was provided by FT-IR spectra for the identification of synthesized nanoparticles. Fig. 3.6 show the FT-IR spectra of Mn_3O_4 and Ni-doped Mn_3O_4 nanoparticles were investigated in the wavenumber range of 500 to 4000 cm^{-1}.

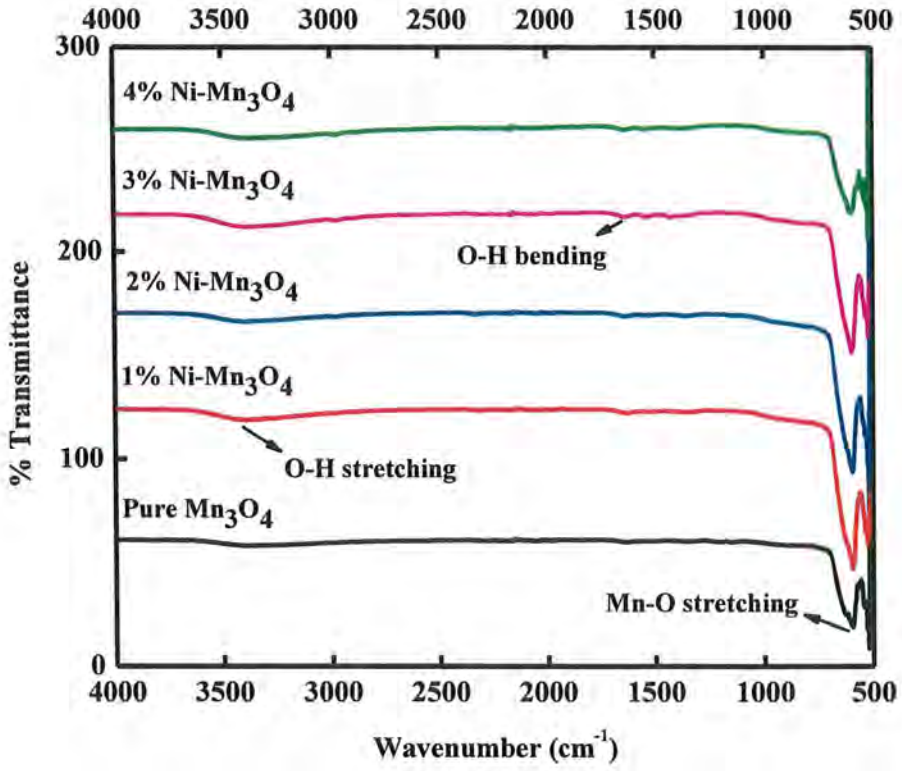

Figure 3.6: FT-IR spectrum of pure and (1-4) % Ni-Mn_3O_4 NPs.

The typical band for the Mn-O stretching vibration in tetrahedral sites was visible in the spectrum of Mn_3O_4 NPs at 624 cm^{-1}. While the distortion vibration of Mn-O in an octahedral site is responsible for the vibration frequency.[62].The adsorbed water molecules on the surface of NPs exhibit O-H bending and stretching in weak bands at 1630 cm^{-1} and 3430 cm^{-1}, respectively[63]. With an increase in dopant percentage, the spectra, as shown in Figure 3.6 that did not significantly alter. It verified the substitution of Ni ions for Mn ions while leaving its structural integrity intact. The values of FT-IR peaks and their respective correspondence is given in Table 3.3.

Table 3.3: FT-IR peaks of synthesized pure & doped Mn_3O_4 nanoparticles and their correspondence.

Sr. No.	Wavenumber (cm^{-1})	Mode of vibration
1	3430	O-H stretching
2	624	Mn-O stretching (tetrahedral)
3	1630	O-H bending
4	525	Mn-O distortion vibration (octahedral)

3.4 Photocatalytic degradation of dyes

The photocatalytic degradation of Methyl blue and Methyl orange dye was examined in the presence of sunlight, at room temperature.

3.5 Photocatalytic degradation of Methyl Blue dye by Ni-Mn_3O_4 NPs

First of all, the prepared nanoparticles of pure and Ni-doped Mn_3O_4 were used for the photocatalytic degradation of Methyl blue. This was done to check the photocatalytic activity of the prepared samples for a certain dye. This procedure was performed in the presence of sunlight at room temperature for almost 135 minutes. As it is exposed to sunlight, the dye started degrading. With the passage of time, the peak intensity of the dye solution decreased gradually.

The maximum absorption peak for Methyl blue is at 664 nm. The photocatalytic activity was evaluated at optimal condition by examining certain factors. These factors include dopant optimization, dosage of catalyst, concentration of dye, and Ph. The factors are discussed below one by one.

3.5.1 Dopant optimization

The first step taken in determining the optimum conditions for degradation of dye is the dopant optimization. The absorption peak intensity decreased with time

which assured the degradation of dye. Dye degradation is actually the breaking of chromophore structure of dye. 2 mg of each synthesized catalyst was used in 30 μM concentration of dye solution.

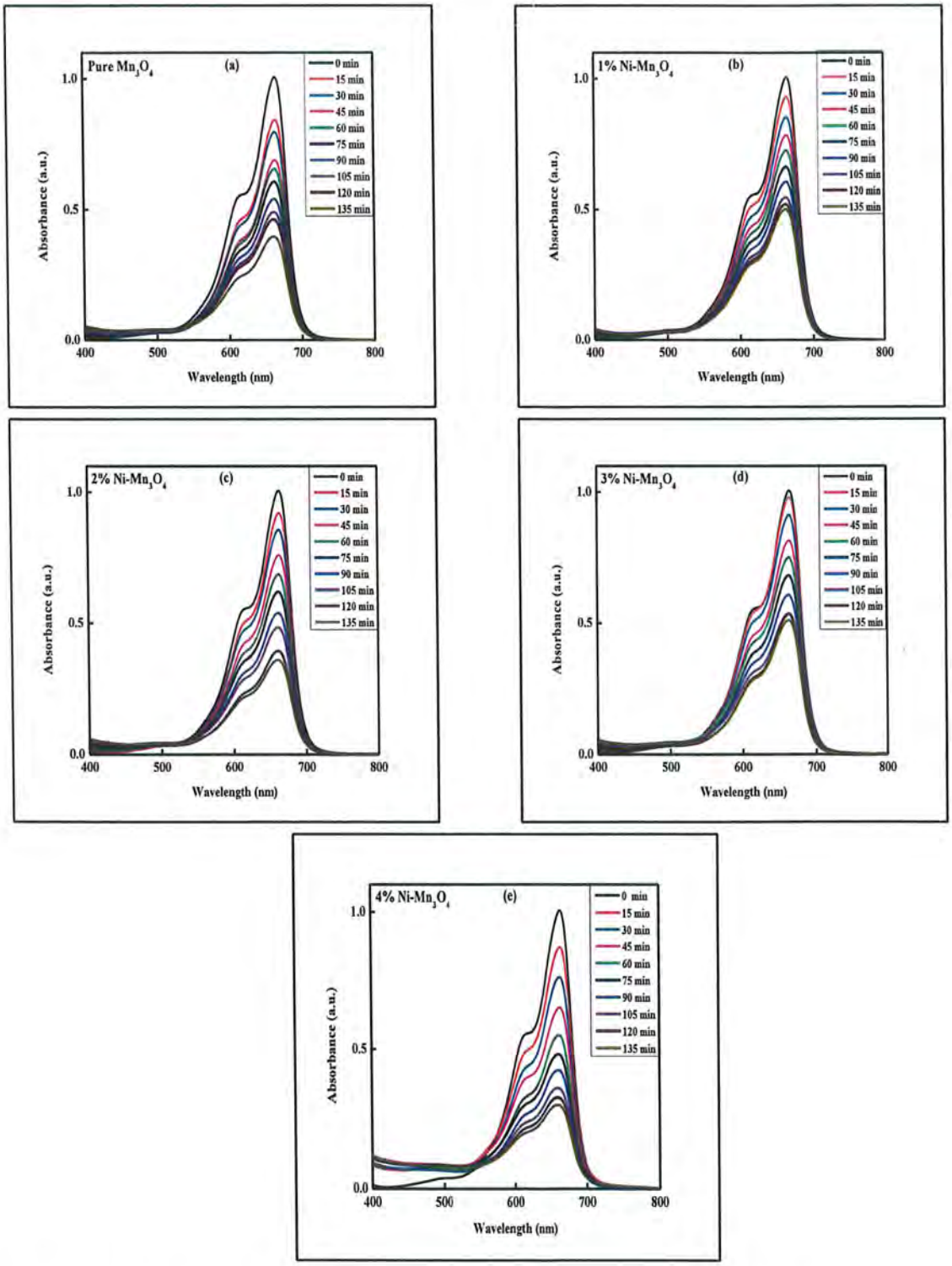

Figure 3.7: Absorption spectra of photodegradation of MB dye by Mn_3O_4 and (1-4) % Ni-Mn_3O_4 NPs.

Within the time interval of 135 minutes, the color of dye solution was also faded. The UV-Visible spectra of Methyl blue degradation by pristine Mn_3O_4 and Ni-doped Mn_3O_4 is shown in Fig. 3.7.

The photocatalytic activity of synthesized catalysts depend on the adsorbing ability of the dye molecules on the surface of catalyst. The percentage Photodegradation efficiency (%PDE) for pure Mn_3O_4 and (1-4) % weighted percentage of Ni-doped Mn_3O_4 nanoparticles was observed. Figure shows that the maximum photodegradation efficiency was for 4 % Ni-Mn_3O_4 NPs. It may be due to less e^-/h^+ recombination which is due to an increase in surface states produced by Ni ions.

Dye degradation directly depend on the amount of catalyst adsorbed on its surface. An increase in %PDE is caused by more dye molecules adhering to the catalyst's surface as shown in Fig. 3.8.

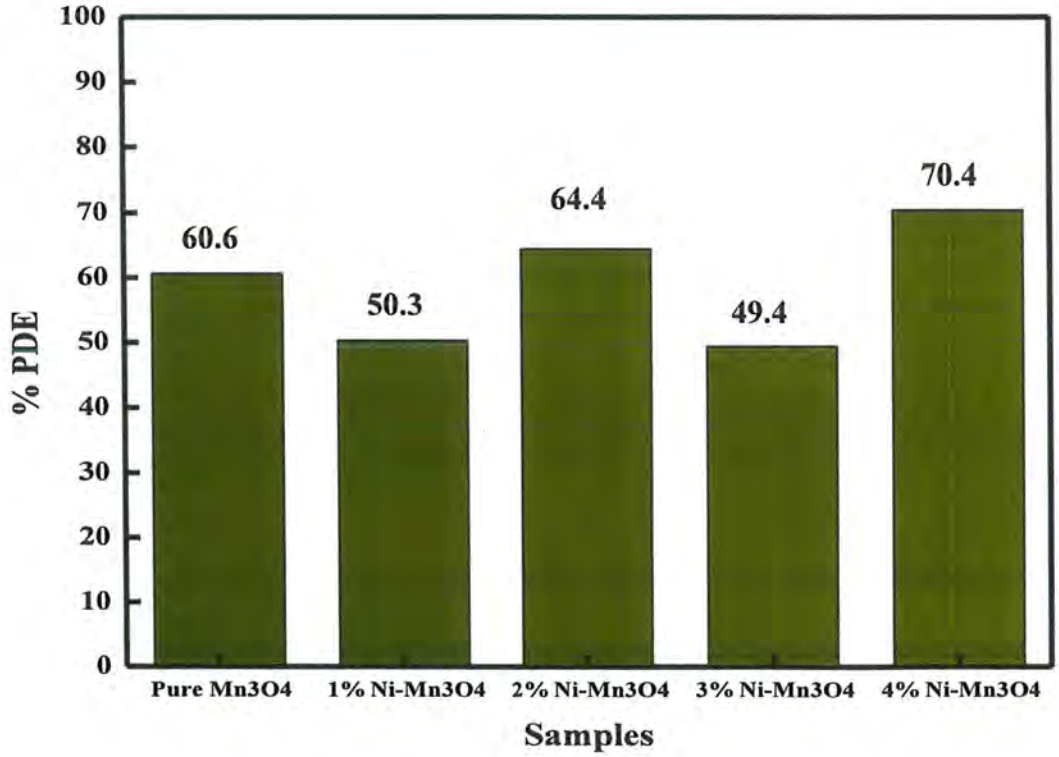

Figure 3.8: %PDE of degradation of MB dye by Mn_3O_4 and (1-4) % Ni-Mn_3O_4 NPs.

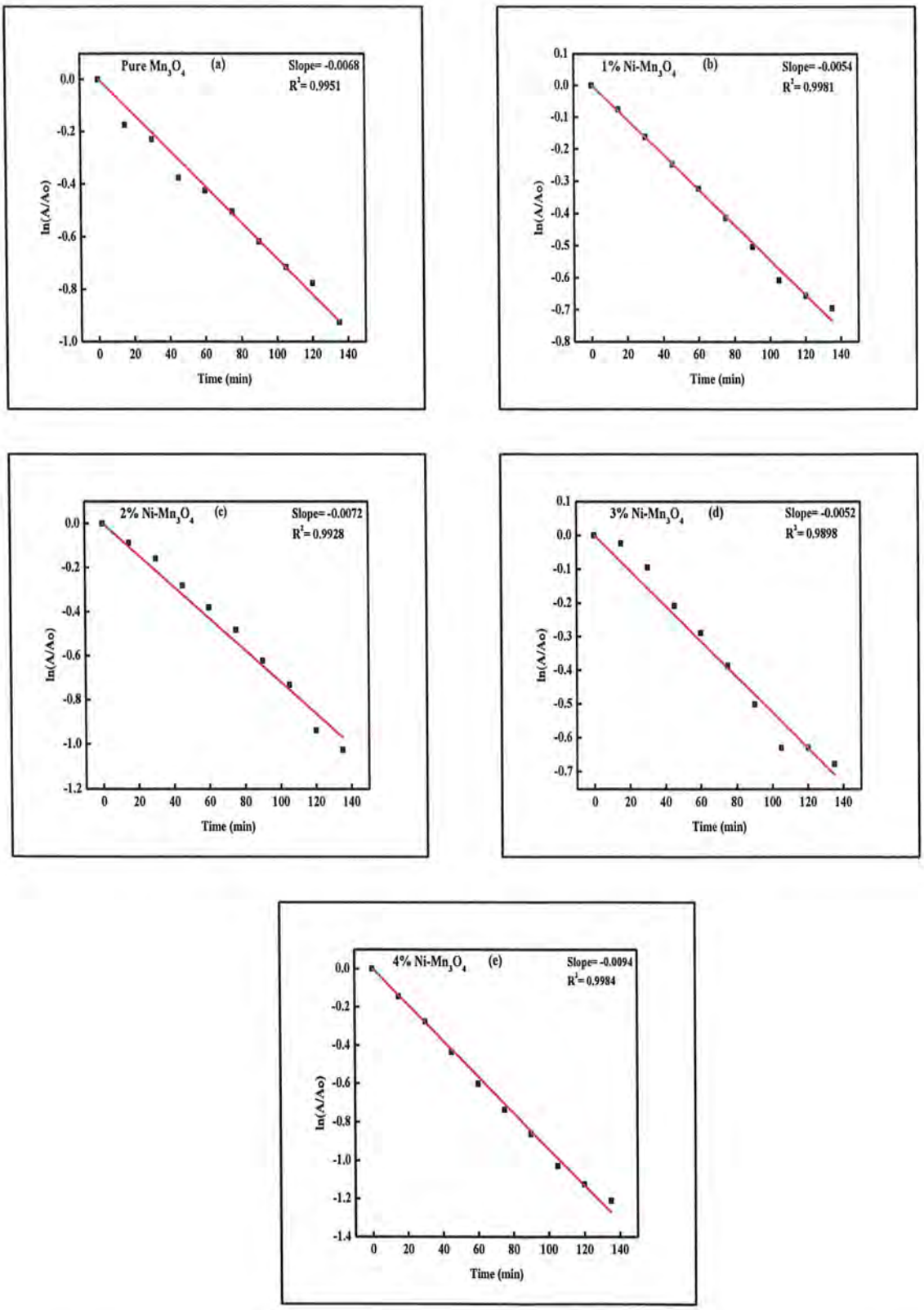

Figure 3.9: Determination of observed rate constant for photodegradation of MB dye by Mn_3O_4 and (1-4) % Ni-Mn_3O_4 NPs.

The concentration of dye is degraded on exposure to sunlight. The graphs show a decrease in the ratio of A/A_0 with increase in time. All these parameters suggest that degradation of dyes follow pseudo first order kinetics as shown in Fig. 3.9. The kinetic parameters are calculated as given in the Table 3.4.

Table 3.4: Weighted percentage of Ni-Mn_3O_4 NPs, % PDE, rate constant (k) for MB dye photocatalytic degradation.

Sr. No.	Sample	%PDE	Kinetic rate constant (min^{-1})	Half-life (min)	R^2
1	Pure Mn_3O_4	60.6	6.8×10^{-3}	101.91	0.9951
2	1% Ni-Mn_3O_4	50.3	5.4×10^{-3}	128.33	0.9981
3	2% Ni-Mn_3O_4	64.4	7.2×10^{-3}	96.25	0.9928
4	3% Ni-Mn_3O_4	49.4	5.2×10^{-3}	133.26	0.9898
5	4% Ni-Mn_3O_4	70.4	9.4×10^{-3}	73.72	0.9984

3.5.2 Effect of dosage of catalyst

After optimizing the catalyst we found the dose of optimized catalyst by taking different amount of that catalyst in the same dye solution. So, second step was the investigation of the effect of catalyst on the degradation efficiency. To find the optimal conditions for catalyst dosage, different amounts of optimized catalyst were added in 30 μM concentration of methyl blue dye solution.

4 % Ni-Mn_3O_4 NPs showed significant photodegradation efficiency so the dye solutions were investigated with dosage of this catalyst ranging from 1 to 4 mg. Figure 3.10 shows the intensity of peaks for different catalyst dosages.

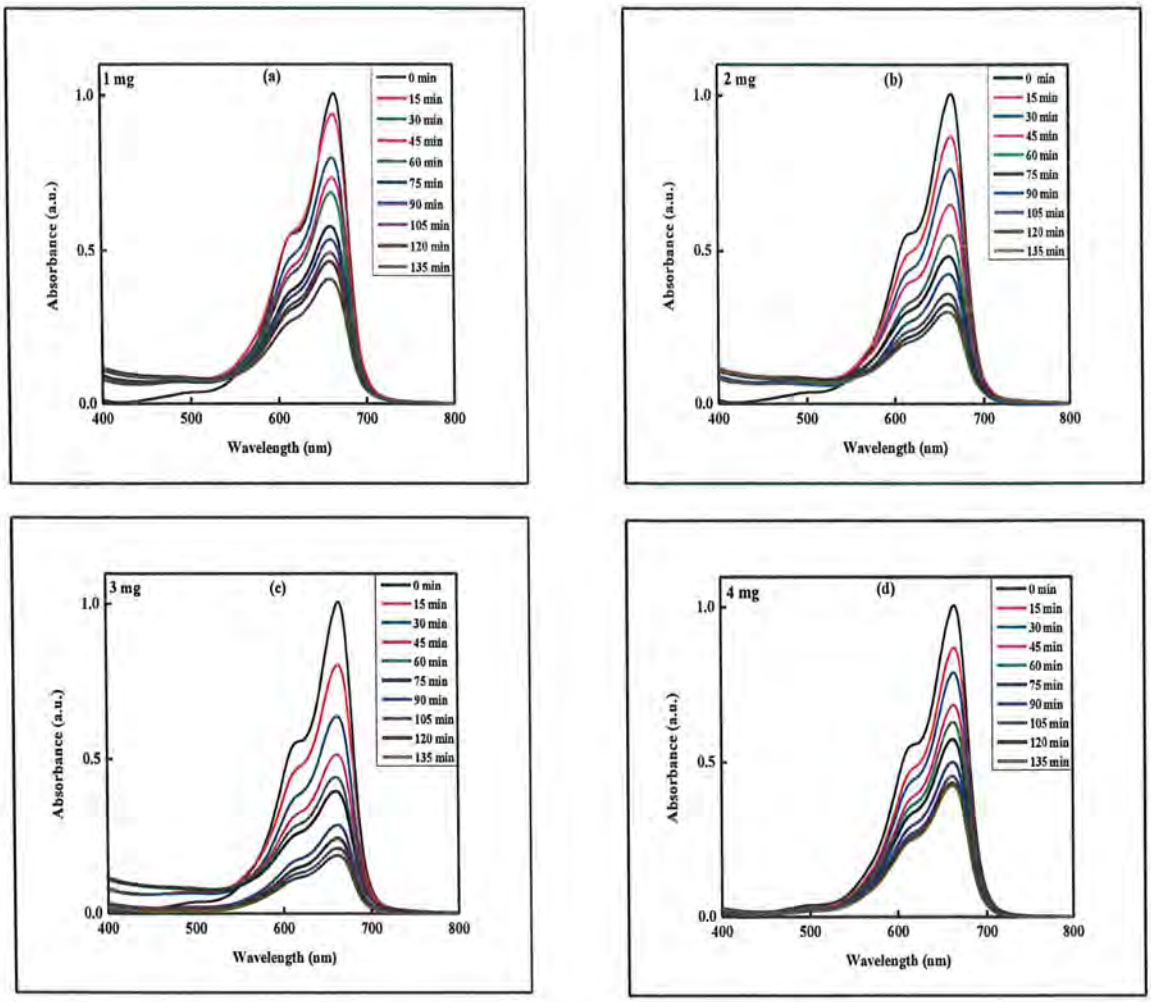

Figure 3.10: Photodegradation of MB dye by different amounts of 4% Ni-Mn_3O_4 photocatalyst.

Addition of more catalyst showed a prominent change in the degradation of dyes. 3 mg of 4 % catalyst showed maximum %PDE for the photocatalytic degradation of MB dye as shown in Fig. 3.11. This is because there are active sites on the catalyst surface and UV light can enter the solution because of increased light scattering and screening[64]. As the concentration of catalyst is raised to 4 mg, the rate of degradation is decreased. This is by overlapped adsorption sites caused by adsorbent overpopulation and deactivation of activated catalyst particles brought on by impact with ground state catalyst. Dye molecules collided and caused the deactivation of active sites due to which there is less absorption of photons of light.

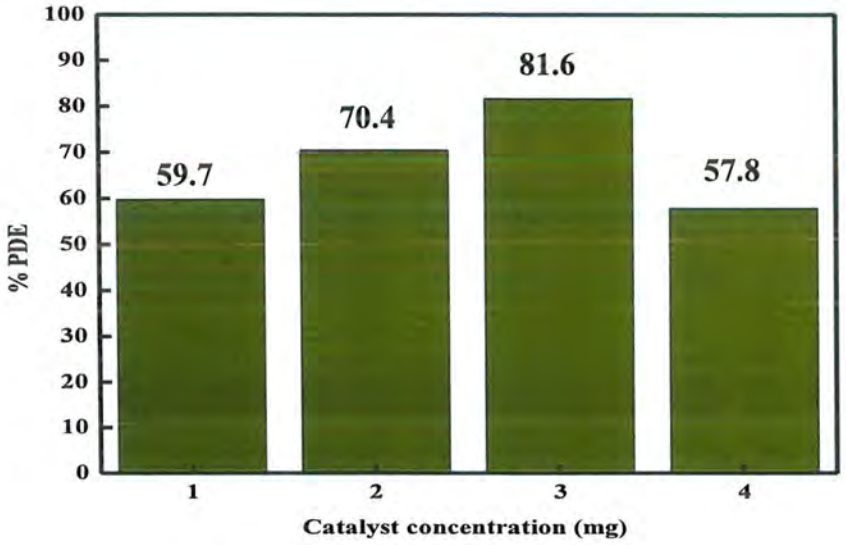

Figure 3.11: %PDE of degradation of MB dye by 4 % Ni-Mn_3O_4 NPs.

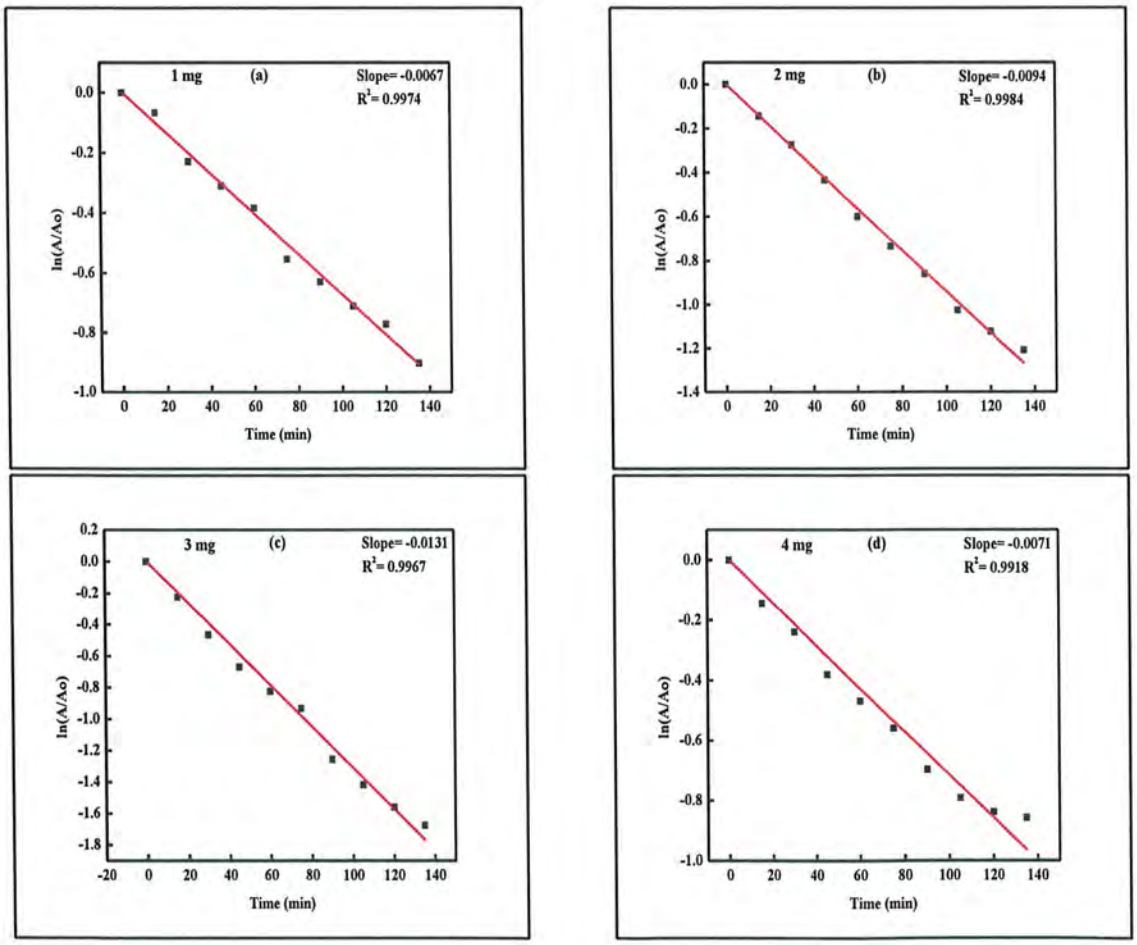

Figure 3.12: Rate constants for degradation of MB dye by different amounts of 4% Ni-Mn_3O_4 photocatalyst.

It is concluded from these graphs in Fig. 3.12 that pseudo first order kinetics is followed in all these reactions. The kinetic data is given in the Table 3.5.

Table 3.5: Amount of 4 % Ni-Mn_3O_4 NPs, % PDE, rate constant (k) for MB dye photocatalytic degradation.

Sr. No.	Catalyst dosage (mg)	%PDE	Kinetic rate constant (min^{-1})	Half-life (min)	R^2
1	1 mg	59.7	6.7×10^{-3}	103.43	0.9974
2	2 mg	70.4	9.4×10^{-3}	73.72	0.9984
3	3 mg	81.6	1.3×10^{-3}	52.90	0.9967
4	4 mg	57.8	7.1×10^{-3}	97.60	0.9918

3.5.3 Effect of concentration of dye

By using the already optimized amount of the catalyst, concentration of dye was studied. Three different concentrations ranging from 25-35 μM of MB dye were used for the optimization. Absorption spectra for the degradation of dyes at different concentrations is shown in Fig. 3.13. In all of the three solutions, 3 mg of 4 % Ni-Mn_3O_4 NPs were used. There is an increase in photodegradation efficiency with an increase in concentration from 25-30 μM from 49.6 to 81.6 %, respectively. For 35 μM, a decrease in photodegradation efficiency was observed.

The absorption spectra showed different degradation efficiency percentages at different concentrations. Free radical (·OH) generated on the surface of the catalyst play an important role. Higher dye concentrations resulted a decrease in ·OH radical production on the catalyst's surface, which in turn resulted in lower degradation rates.

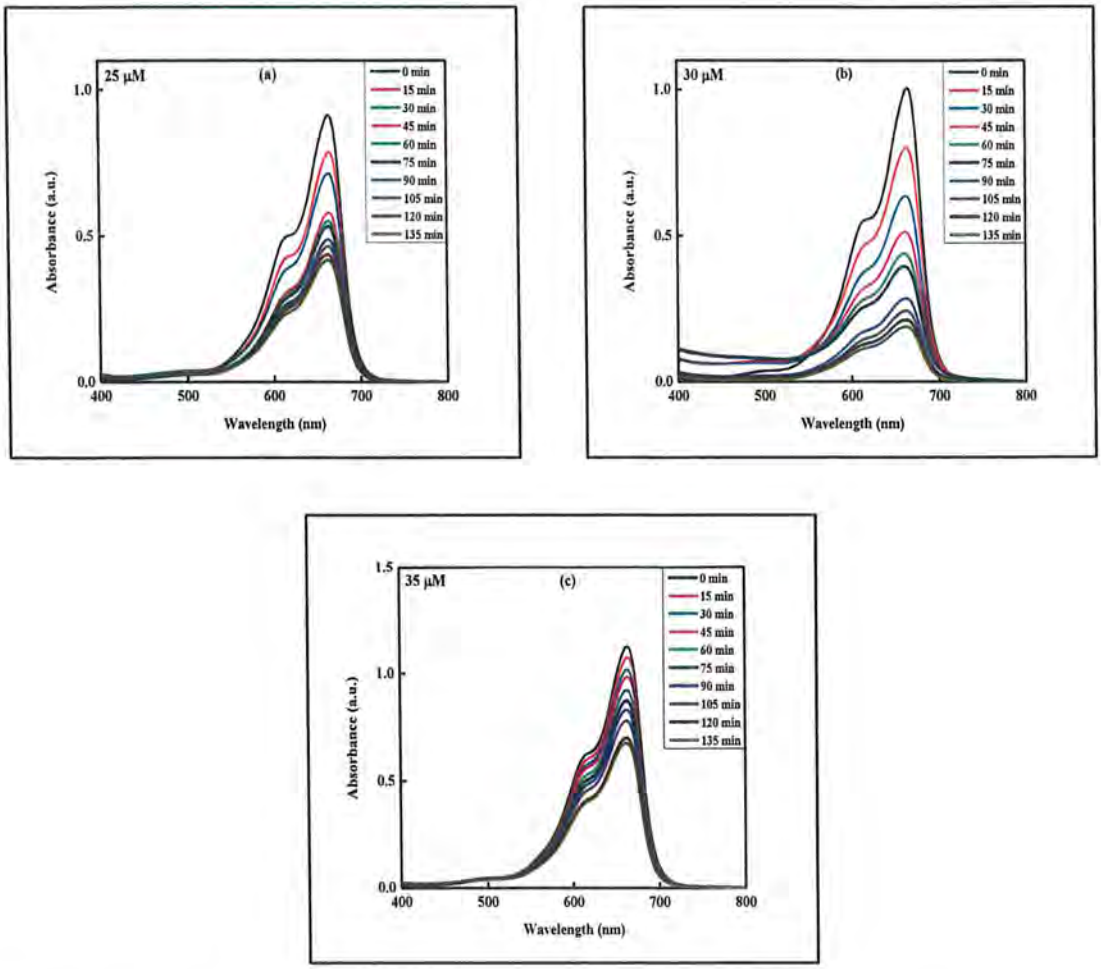

Figure 3.13: Absorption spectra of photocatalytic degradation of different concentrations of MB dye by 4% Ni-Mn_3O_4 NPs.

Availability of active sites at high concentration of dye is less due to which degradation is slow. It might be due the shorter path length of UV light which speeds up the process of degradation. Before reaching the catalyst, some photons may be absorbed by the dye, which can also lower the catalytic efficiency[65].

%PDE is less for low concentration of dye because it is insufficient to adsorb on the catalyst's surface. Deactivation of activated molecules may also cause a decrease in catalytic performance of dyes. The %PDE is shown in Fig. 3.14

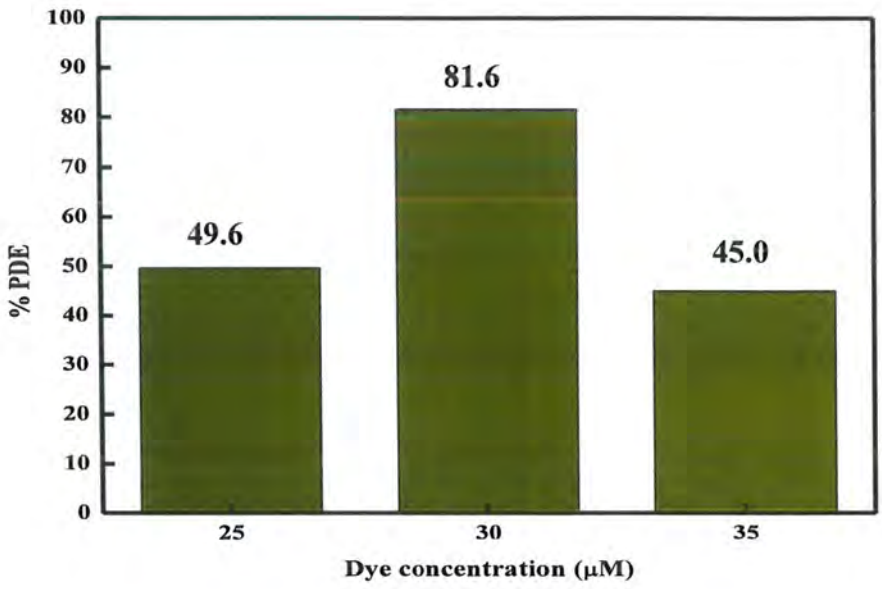

Figure 3.14: %PDE for photodegradation of different concentrations of MB dye.

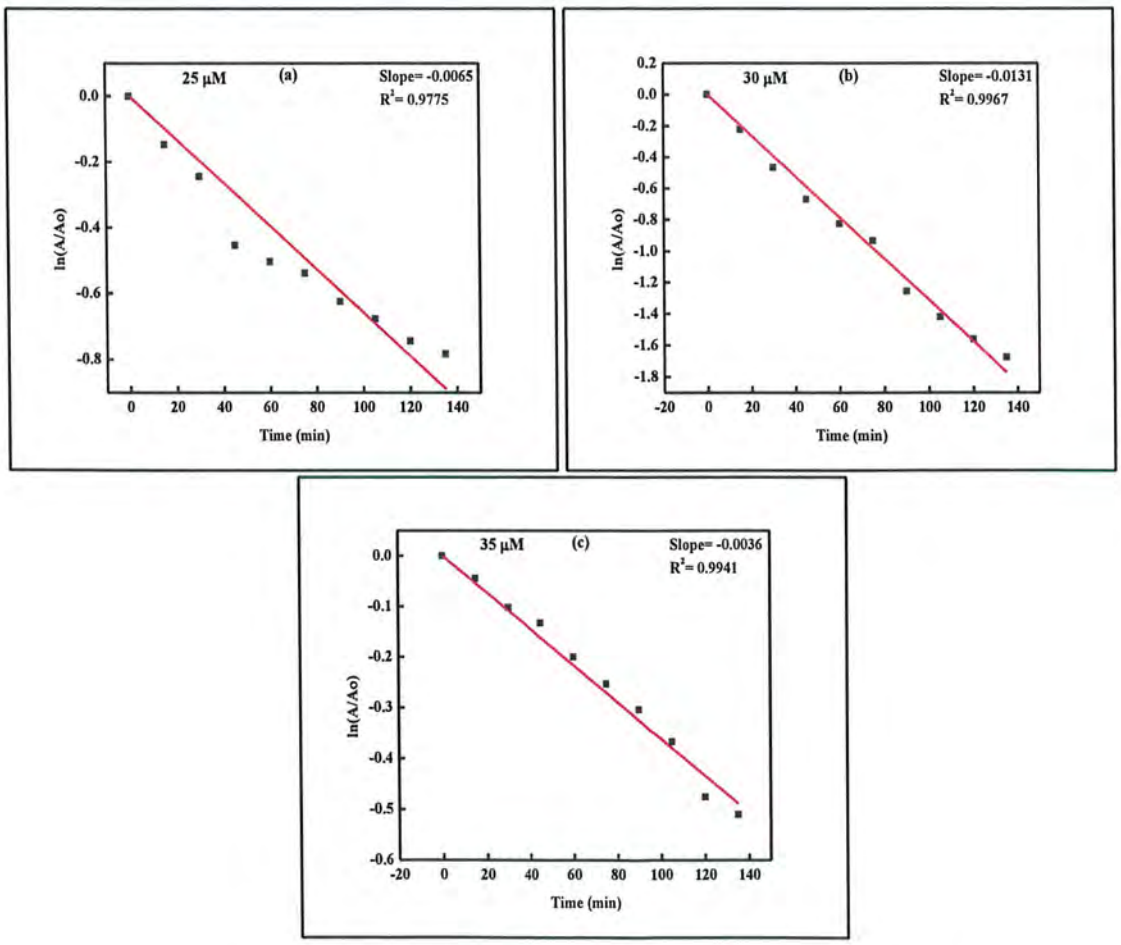

Figure 3.15: Rate constants for different concentrations of MB dye.

Figure 3.15 data showed the pseudo first order kinetics followed by all reactions. Half-life and %PDE of above discussed parameter is given in Table 3.6.

Table 3.6: Dye concentration, % PDE, kinetic rate constant (k) for the photocatalytic degradation of MB dye.

Sr. No.	Catalyst dosage (μM)	%PDE	Kinetic rate constant (min^{-1})	Half-life (min)	R^2
1	25 μM	49.6	6.5×10^{-3}	106.61	0.9775
2	30 μM	81.6	1.3×10^{-2}	52.90	0.9967
3	35 μM	45.0	3.6×10^{-3}	192.50	0.9941

3.5.4 Effect of pH

Photocatalytic activity of dyes mostly depend on the effect of pH. The effect of pH was studied by making different solutions at pH values varying from 3 to 11. HCl and NaOH were used to adjust the pH of acidic and basic solutions. All these solution have optimized amount of catalyst having fixed amount of dye concentration that is 3 mg of 4 % Ni-Mn_3O_4 catalyst. Absorption spectra of solutions at different pH values are shown in Fig. 3.16.

The percentage degradation efficiency for lower pH values is less as compared to higher pH values shown in Fig 3.17. 95.3 % of dye is degraded at pH 11 in basic medium. Methyl blue is a cationic dye. Negative charge is formed on the catalyst surface at higher pH levels. The negatively charged catalyst surface and the MB cation are strongly attracted to one another by electrostatic forces of attraction. The oxidation process that occurs in an alkaline solution is primarily caused by hydroxyl radicals (·OH). Thus, at pH 11, the surface of catalyst became negatively charged, and MB adsorption takes place which increases the rate of photocatalysis.

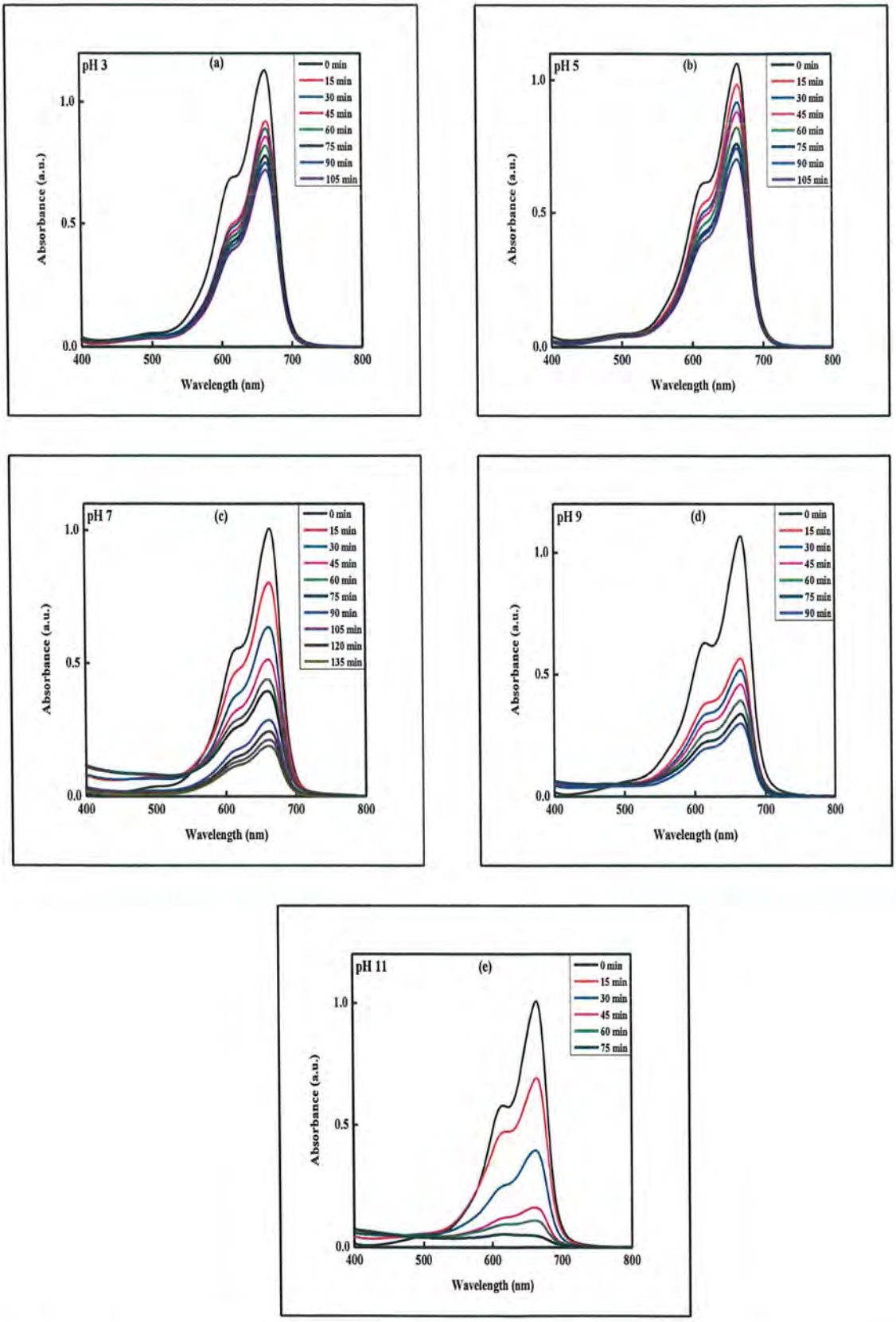

Figure 3.16: Absorption spectra for degradation of MB dye at different pH values by 4% Ni-Mn_3O_4 NPs.

However, at pH 9, the dye is more adsorbed on the surface of synthesized nanoparticles, reducing the surface's exposure to sunlight. As a result, the production of ·OH free radical is decreased. It slowed down the oxidation reaction and reduced the degradation of MB dye[66].

The nanoparticles' ability to aggregate and limit the surface area required for optimal dye adsorption and photon absorption from sunlight, an acidic pH does not demonstrate good degradation efficiency. The positively charged catalyst surface and the methyl blue cation are attracted to one another under acidic pH conditions.

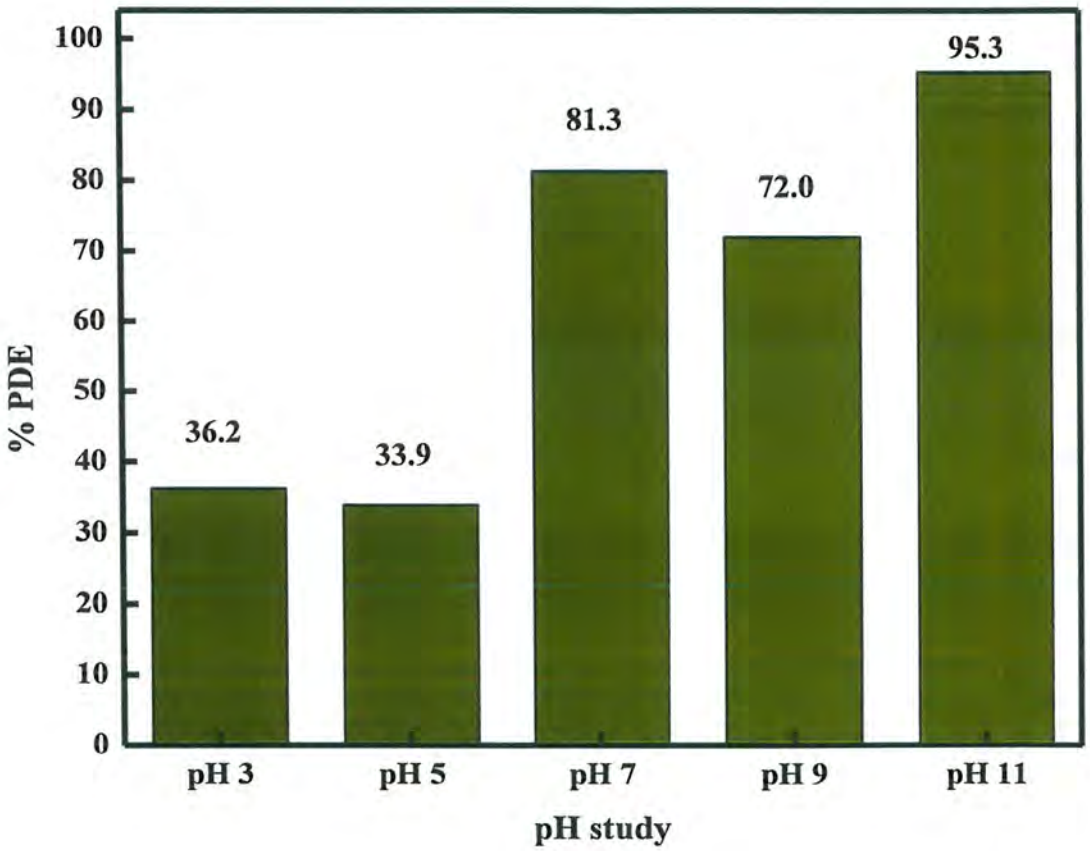

Figure 3.17: Different pH levels for MB dye degradation at different pH values by 4% Ni-Mn_3O_4 photocatalyst.

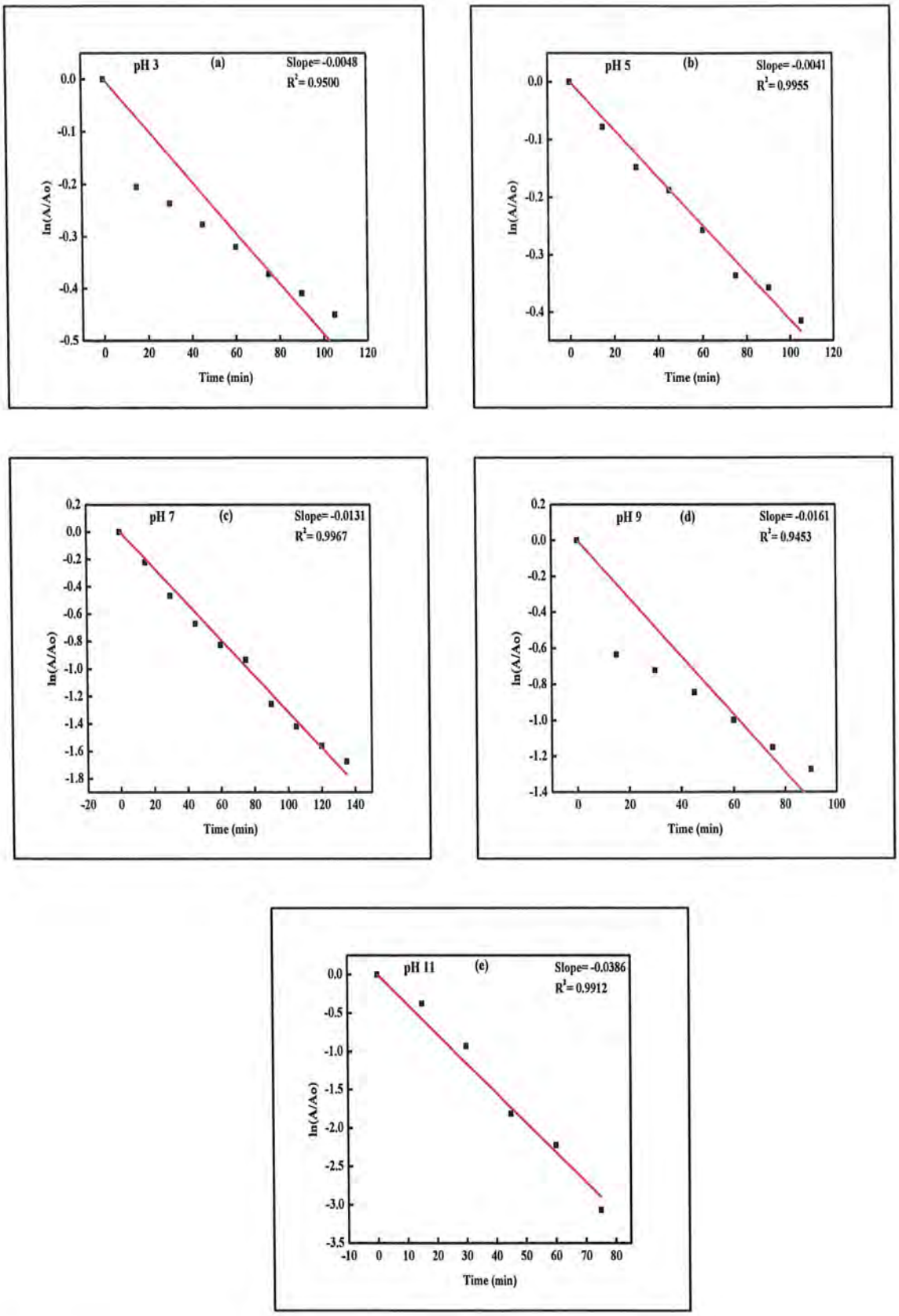

Figure 3.18: Observed rate constant at different pH levels for the degradation of MB dye.

The data in Fig. 3.18 confirmed that all these reactions follow first order kinetics in a satisfactory manner. Table 3.7 enlist the pH, %PDE, half-life and kinetic rate of the degradation of MB dye.

Table 3.7: Data of pH, rate constant (k), % PDE for MB dye photocatalytic degradation by 4% Ni-Mn_3O_4 photocatalyst.

Sr. No.	pH	%PDE	Kinetic rate constant (min^{-1})	Half-life (min)	R^2
1	3	36.2	4.8×10^{-3}	144.37	0.9500
2	5	33.9	4.1×10^{-3}	169.02	0.9955
3	7	81.6	1.3×10^{-2}	52.90	0.9967
4	9	72.0	1.6×10^{-2}	43.04	0.9453
5	11	95.3	3.8×10^{-2}	17.95	0.9912

3.6 Photocatalytic degradation of Methyl Orange by Ni-Mn_3O_4 NPs

The synthesized nanoparticles of pure and Ni-doped Mn_3O_4 were used for the photocatalytic degradation of Methyl orange. The phtotcatalytic activity of the prepared samples for a certain dye were checked. Similarly, this procedure was performed in the presence of sunlight at room temperature like the previous dye. MeO dye showed degradation on exposure to sunlight.

The maximum absorption peak for Methyl orange is at 465nm in UV-Visible spectra. The optimal conditions for the better photocatalytic activity of dye were evaluated by examining certain factors. These factors are dopant optimization, dosage of catalyst, concentration of dye, and pH. First of all, dopant optimization was studied.

3.6.1 Dopant optimization

Above mentioned procedure is repeated for the degradation of this dye. The photocatalytic degradation of MeO dye with synthesized Nickel doped Mn_3O_4

nanoparticles were shown in the Fig 3.19. The chromophore structure of MeO dye was degraded and the absorption peak intensity decreased with time.

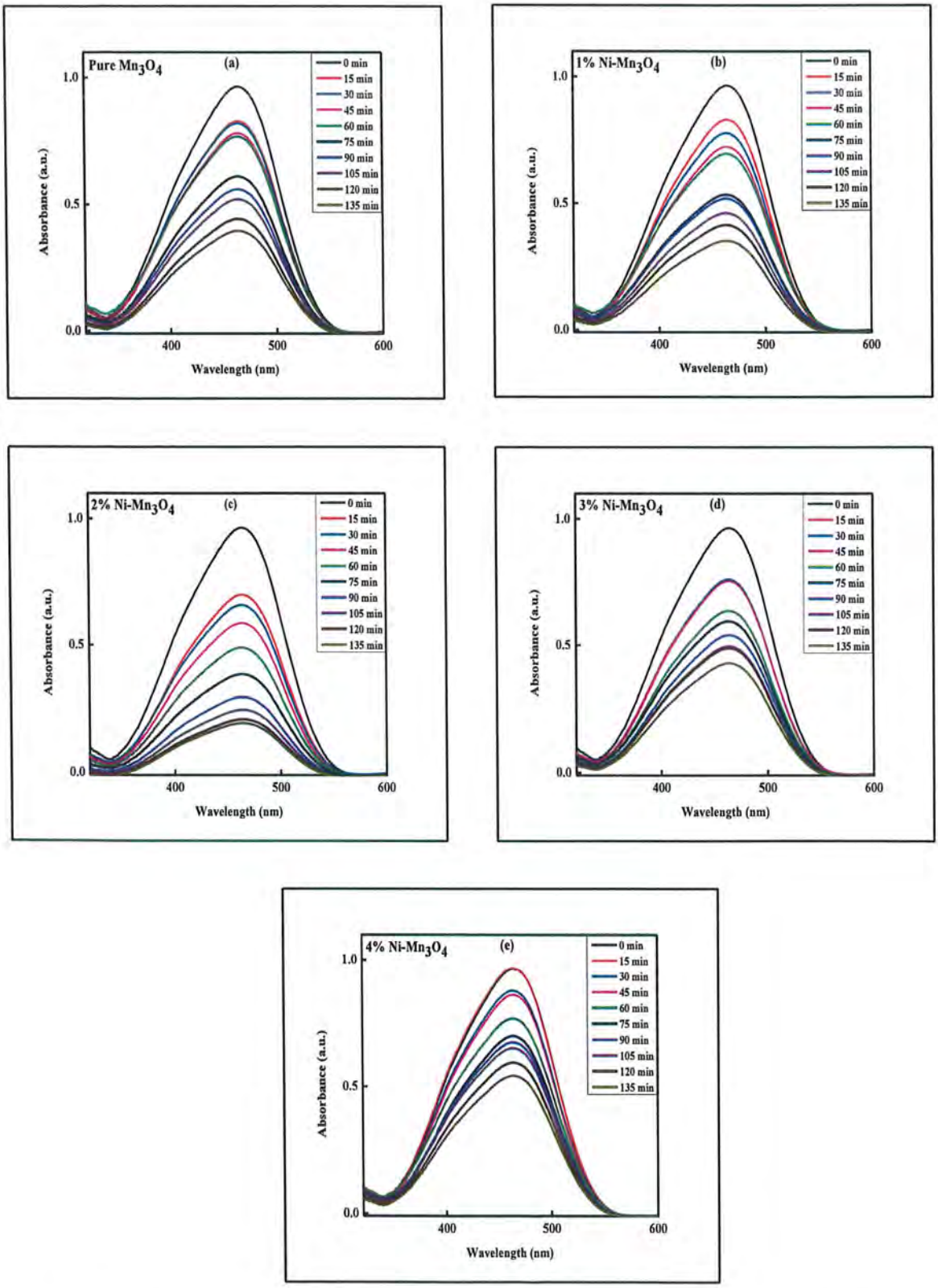

Figure 3.19: Photodegradation of MeO dye by pure and (1-4) % Ni-Mn_3O_4 NPs.

Above figure demonstrated the degradation of Methyl orange dye by various weighted percentages of Nickel doped Mn_3O_4 nanoparticles. The maximum %PDE value for pure Mn_3O_4 NPs was 59 % as shown in Fig 3.20. On the other hand, Ni-doped Mn_3O_4 NPs showed better photocatalytic efficiency. The maximum %PDE for synthesized 2% Ni-Mn_3O_4 NPs was found to be 79.8 %. Many surface defects were discovered as a result of surface functionalization caused by Ni ions, which lowered the rate of e^-/h^+ recombination. More dye molecules are adsorbed on the surface of the catalyst at highest value of %PDE. The agglomeration on the photocatalyst's surface caused the degradation efficiency to decrease as dopant concentration is increased[67].

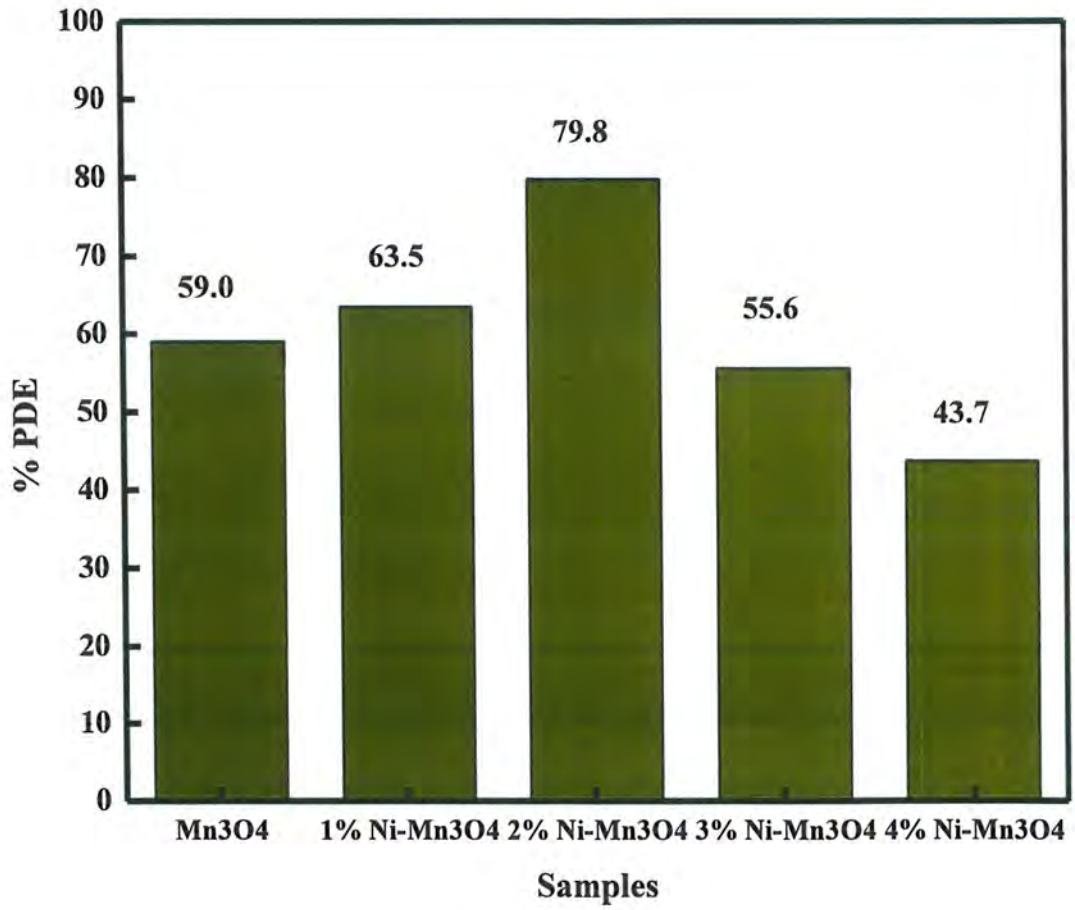

Figure 3.20: %PDE of MeO dye with pure and (1-4) % Ni-Mn_3O_4 NPs.

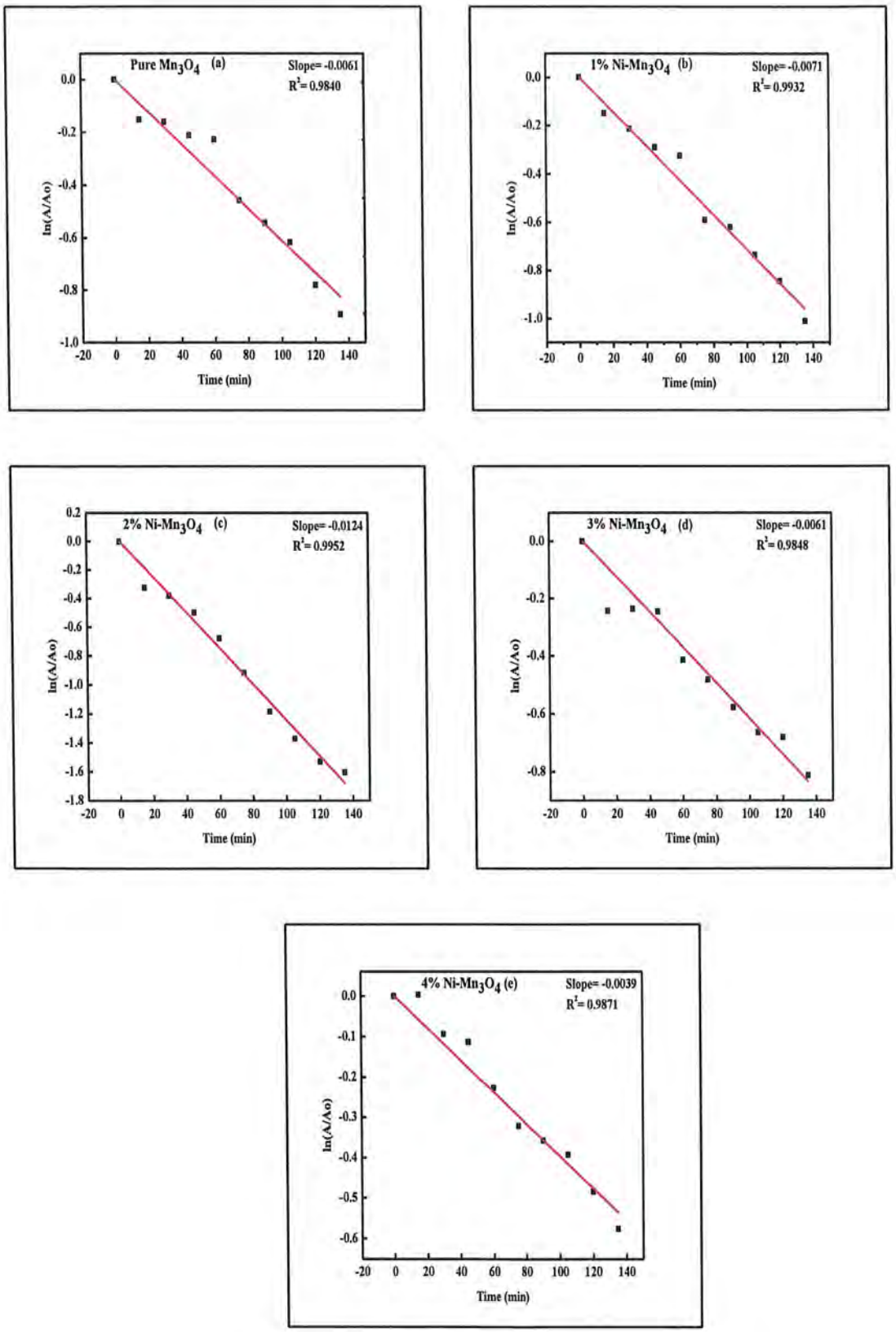

Figure 3.21: Observed rate constant for Photodegradation of MeO dye by Mn_3O_4 and (1-4) % Ni-Mn_3O_4 NPs.

Figure 3.21 showed the photocatalytic degradation of dye follows the pseudo-first order kinetics. The concentration of the dye decreases as the process proceeds. Table 3.8 has the half-life and kinetic data of the above synthesized material.

Table 3.8: Weighted percentage of Ni-Mn_3O_4 NPs, rate constant (k), %PDE for MeO photocatalytic degradation.

Sr. No.	Sample	%PDE	Kinetic rate constant (min^{-1})	Half-life (min)	R^2
1	Pure Mn_3O_4	59.0	6.1×10^{-3}	113.60	0.9840
2	1% Ni-Mn_3O_4	63.5	7.1×10^{-3}	97.60	0.9932
3	2% Ni-Mn_3O_4	79.8	1.2×10^{-2}	55.88	0.9952
4	3% Ni-Mn_3O_4	55.6	6.1×10^{-3}	113.60	0.9848
5	4% Ni-Mn_3O_4	43.7	3.9×10^{-3}	177.69	0.9871

3.6.2 Effect of catalyst dosage

In the next step, the effect of catalyst dosage was investigated on the percent degradation of dye. The optimal dosage of catalyst must be determined to extract the highest amount of organic dye. Due to their excellent photodegradation efficiency, 2 % Ni-Mn_3O_4 was used in all further reactions. The dye concentration was maintained at 80 μM while the catalyst concentration varied from 1 to 4 mg. The absorption spectra of 2 % Ni-Mn_3O_4 NPs at various dose concentrations are shown in Fig. 3.22.

A prominent change is observed by change in the amount of synthesized NPs. Catalyst dosage was increased from 1 to 2 mg, which increased photodegradation efficiency to 79.8 %. The rise in active sites, which dramatically improve interactions between light and methyl orange dye molecules.

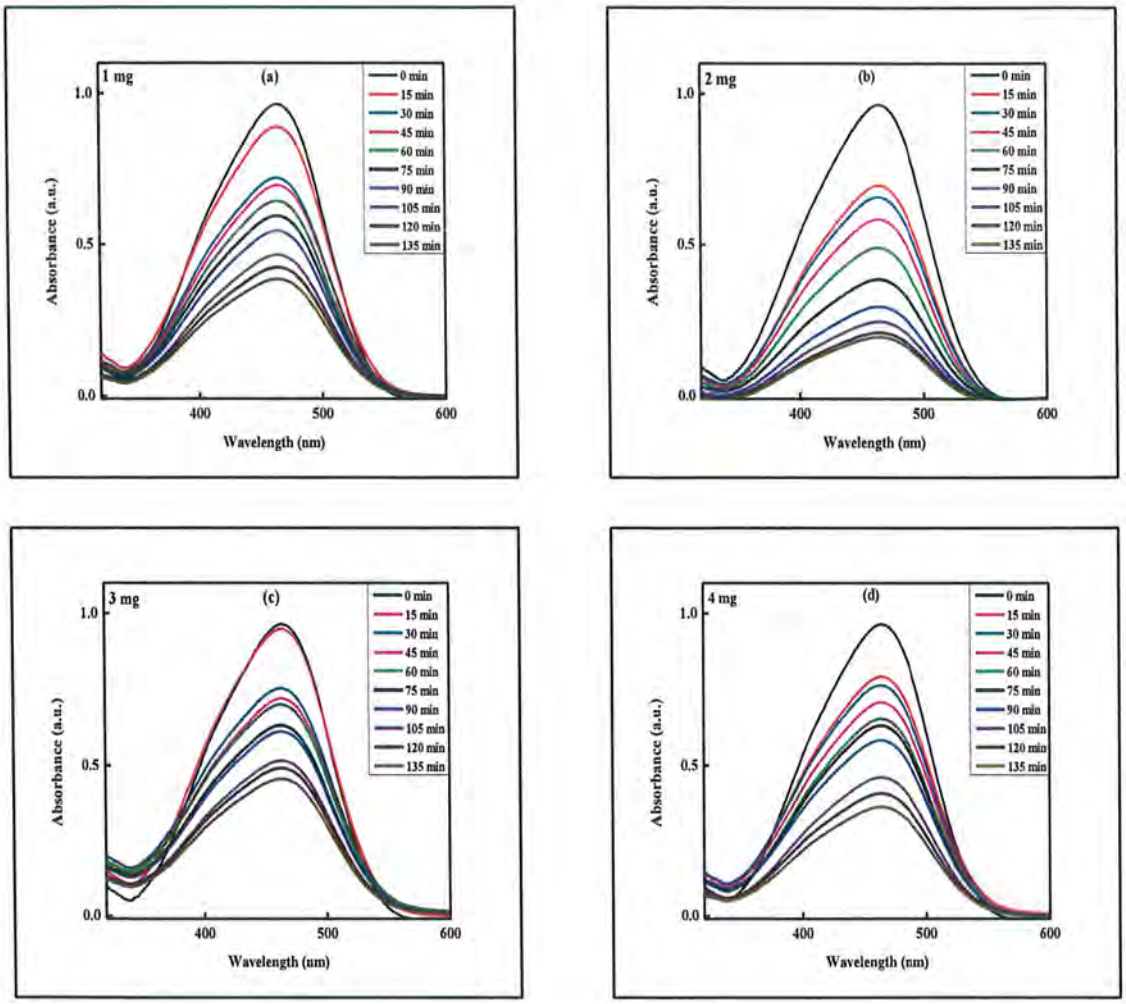

Figure 3.22: Absorption spectra for the Photodegradation of MeO dye by different dosage of 2 % Ni-Mn_3O_4 NPs.

The presence of functional groups enhanced that can be used to explain why degradation efficiency has increased. However, going beyond 2 mg of catalyst had a detrimental effect since the photodegradation efficiency fell to 52.8 %. This is linked to the accumulation of catalyst, which prevents photon absorption on the surface. Additionally, the suspension's turbidity causes less UV radiation to penetrate it, which lowers the effectiveness of photodegradation. Methyl orange showed barely any degradation in the absence of a catalyst, demonstrating the crucial part that a catalyst plays in the photodegradation process. The %PDE is shown in Fig. 3.23.

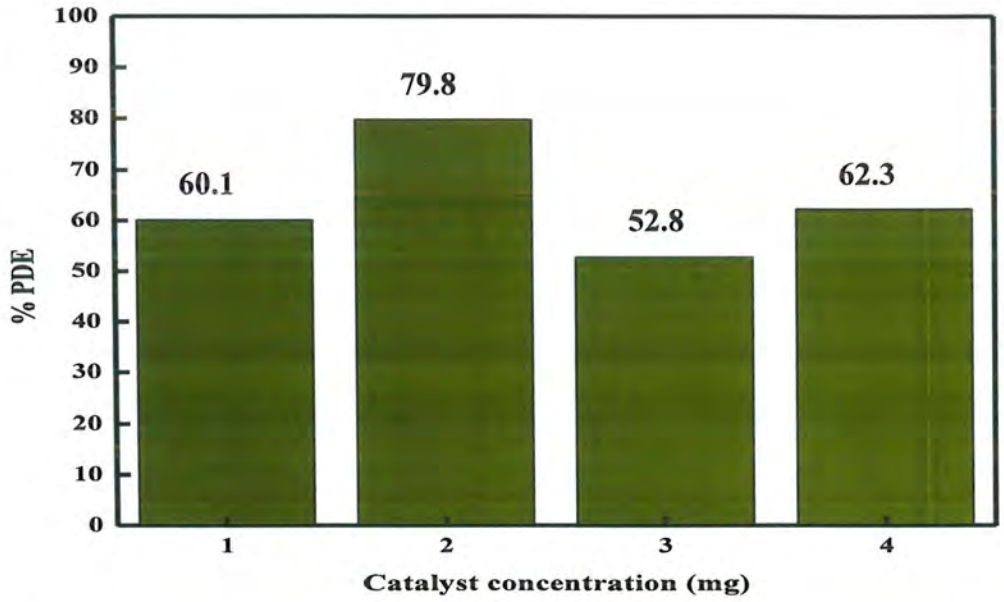

Figure 3.23: %PDE for degradation of MeO dye by different dosage of 2 % Ni-Mn_3O_4 NPs.

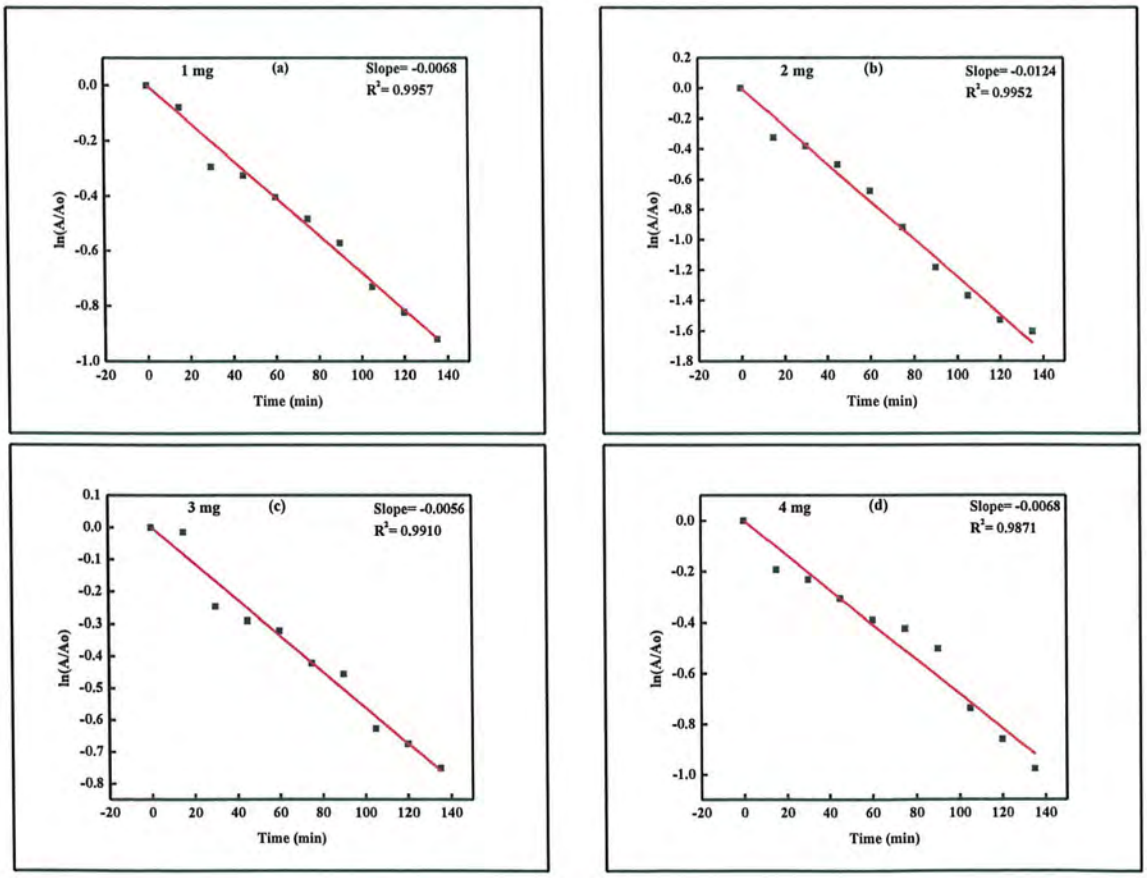

Figure 3.24: Observed rate constant for different amount of 2 % Ni-Mn_3O_4 NPs.

Figure 3.24 showed the photocatalytic degradation of dye follows the pseudo-first order kinetics. Table 3.9 has the half-life and kinetic data of the above synthesized material.

Table 3.9: Different amount of 2 % Ni-Mn_3O_4 NPs, rate constant (k), %PDE for MeO dye degradation.

Sr. No.	Catalyst dosage (mg)	%PDE	Kinetic rate constant (min^{-1})	Half-life (min)	R^2
1	1 mg	60.1	6.8×10^{-3}	101.91	0.9957
2	2 mg	79.8	1.2×10^{-2}	55.88	0.9952
3	3 mg	52.8	5.6×10^{-3}	123.75	0.9910
4	4 mg	62.3	6.8×10^{-3}	101.91	0.9871

3.6.3 Effect of concentration of dye

Furthermore, the photodegradation of MeO dye was investigated at different concentrations ranging from 70 to 90 μM in the presence of a fixed amount of catalyst. The 2 mg amount of 2 % Ni-Mn_3O_4 NPs were used in the manner described above. Figure 3.25 displays the absorption spectra of different dye concentrations. The absorption peak intensity decreases with time.

The absorption spectra showed different degradation efficiency percentages at different concentrations. High concentration of dye resulted a decrease in ·OH radical production on the catalyst's surface, which in turn resulted in lower degradation rates. At high concentration of dye less active sites are available due to which degradation is slow. Before reaching the catalyst, some photons may be absorbed by the dye, which can also lower the catalytic efficiency.

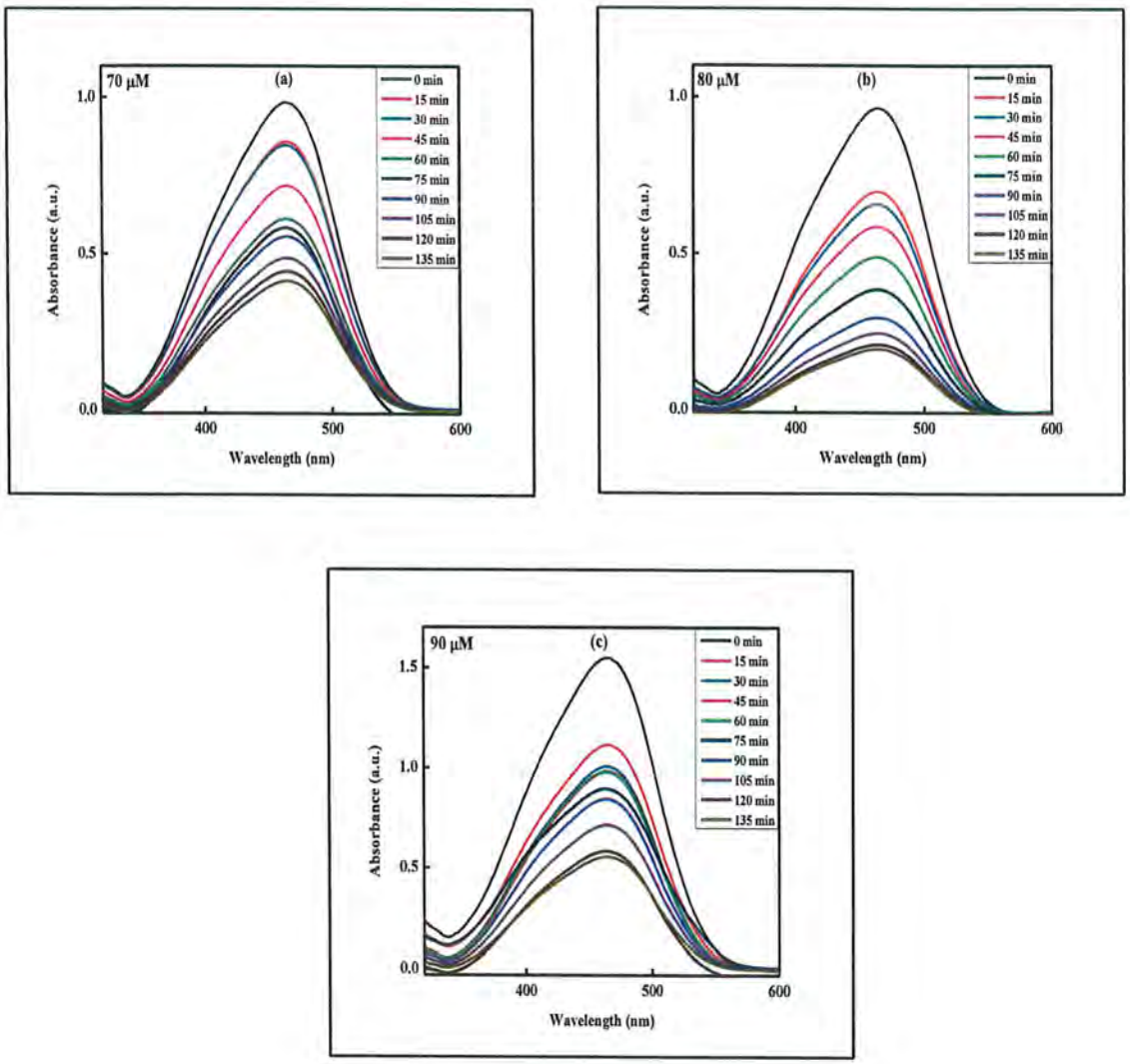

Figure 3.25: Absorption spectra of photocatalytic degradation of MeO dye of different concentrations with 2 mg of 2 % Ni-Mn_3O_4 NPs.

The %PDE for MeO dye is shown in Fig 3.26. %PDE is less for low concentration of dye because it is insufficient to adsorb on the catalyst's surface and there are less active sites availability. Deactivation of activated molecules may also cause a decrease in catalytic performance of dyes. Figure 3.27 showed the photocatalytic degradation of dye follows the pseudo-first order kinetics.

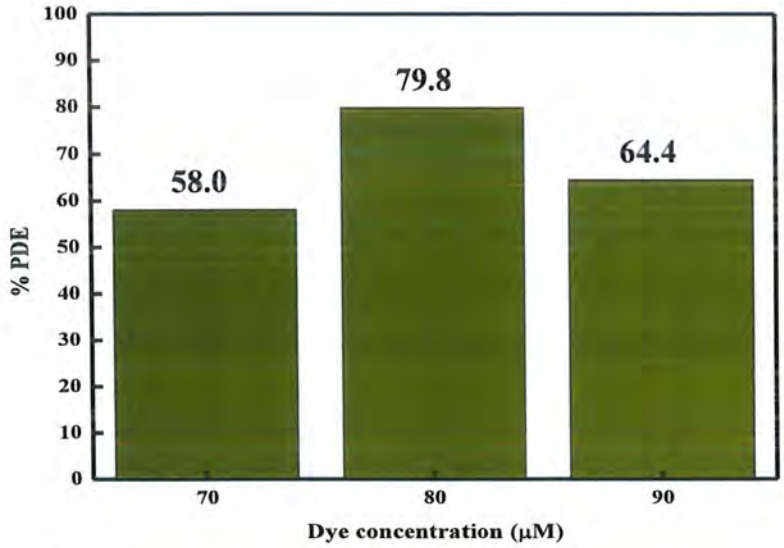

Figure 3.26: Study of %PDE at different concentrations of MeO dye.

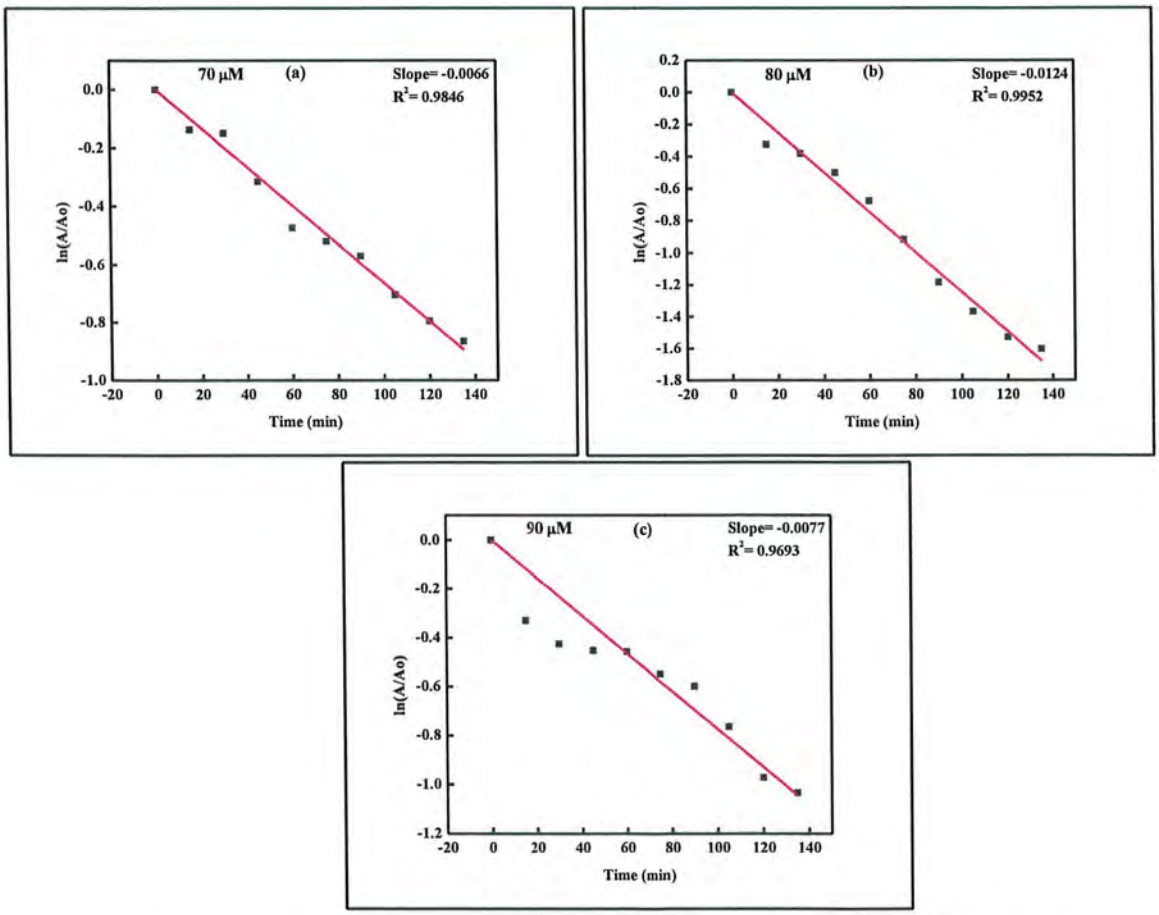

Figure 3.27: Study of rate constant at different concentrations of MeO dye.

The concentration of the dye decreases with time interval. Table 3.10 has the half-life and kinetic data of the above synthesized material.

Table 3.10: Different MeO dye concentration, rate constant (k), %PDE for photocatalytic degradation.

Sr. No.	Dye concentration (μM)	%PDE	Kinetic rate constant (min^{-1})	Half-life (min)	R^2
1	70 μM	58.0	0.6×10^{-2}	105.00	0.9846
2	80 μM	79.8	1.2×10^{-2}	55.88	0.9952
3	90 μM	64.4	0.7×10^{-2}	90.00	0.9693

3.6.4 Effect of pH

This parameter is the most significant in the study of photodegradation. H_2SO_4 and NaOH were used to modify the pH of the solution while keeping the amount of photocatalyst and dye solution concentrations constant. 2 mg of 2 % Ni-Mn_3O_4 nanoparticles were treated with the optimum dye concentration. The system was exposed to light irradiation at pH ranges from 3 to 11. The UV-Visible spectra of MeO dye degraded at various pH 3 and 5 are shown Fig. 3.28.

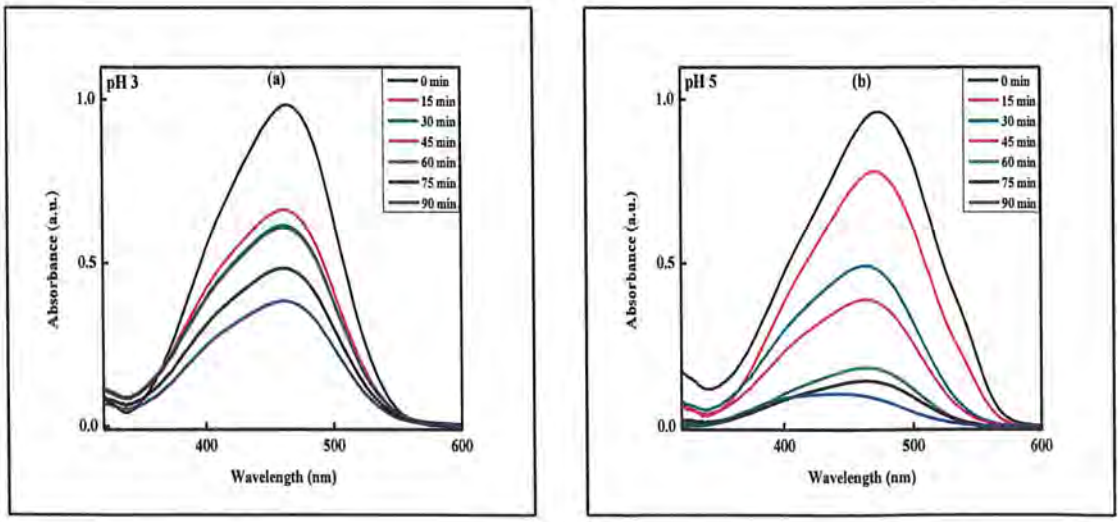

Figure 3.28: Absorption spectra of MeO dye at pH 3 and 5.

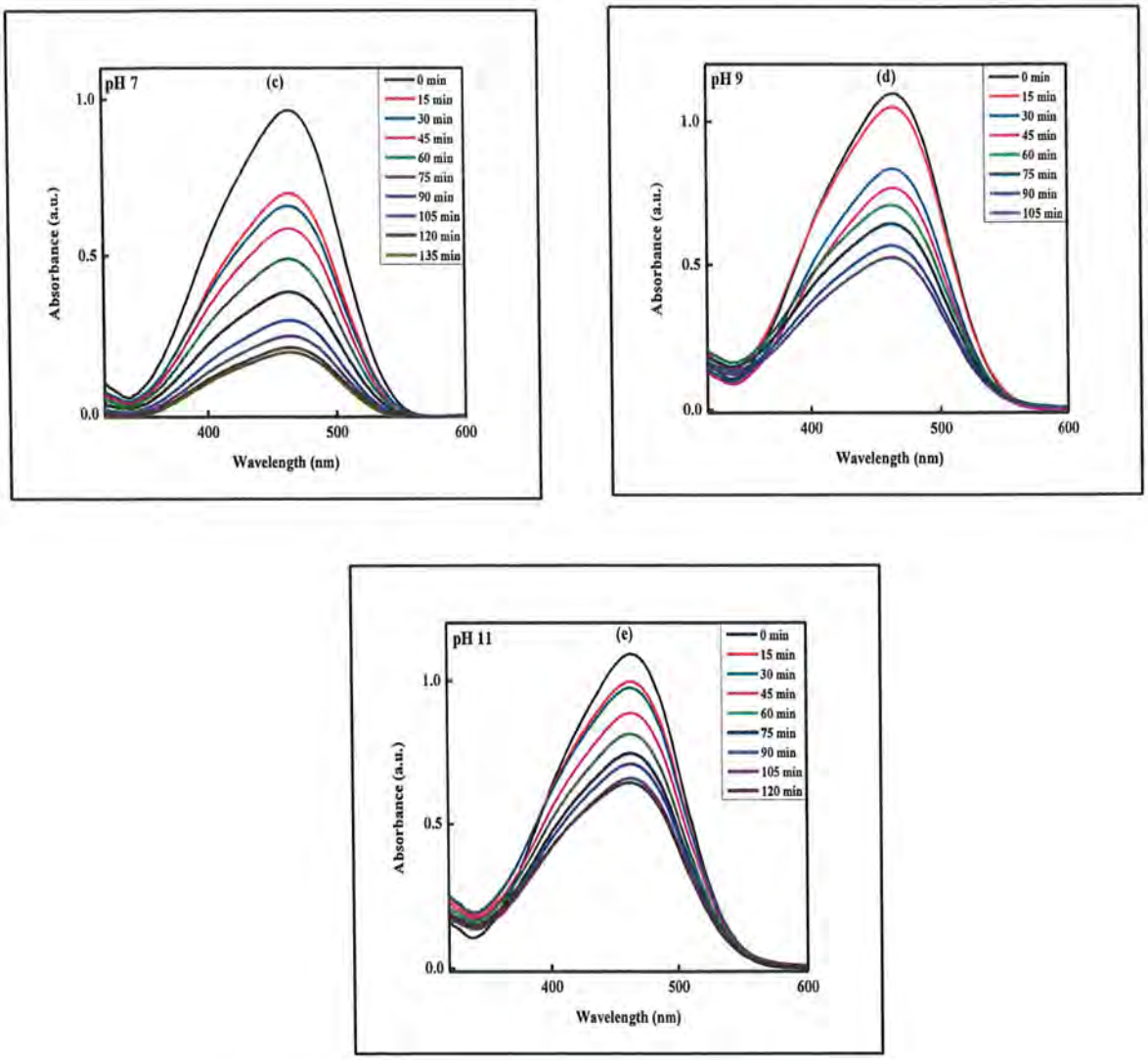

Figure 3.29: Absorption spectra of MeO dye at pH 7, 9 and 11 for degradation.

The color of MeO dye solution changed from orange to red at pH less than 3. This would cause a change in its chemical structure. The chromophore group alters as a result of this chemical structural modification, potentially making the molecule less susceptible to breakdown in the presence of reactive NPs. According to the observed photodegradation, low photocatalytic rates were observed at acidic pH range. Although %PDE was shown to be at its maximum at pH 5. This revealed that less acidic conditions are far more favourable for the production of the reactive intermediates that is hydroxyl free radicals, which further aids in increasing the reaction rate[68]. The ionization of the surface of catalyst and deprotonation of MeO form H^+ ions that are

responsible for photocatalytic activity. High acidic conditions are less favourable and less spontaneous for the formation of reactive intermediates. .

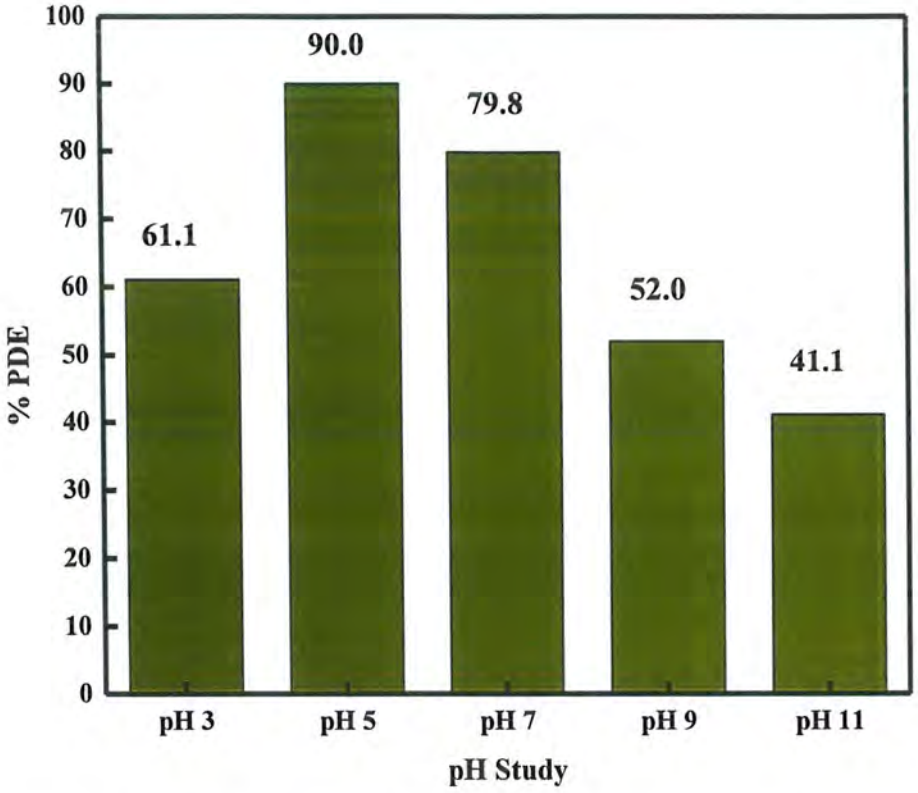

Figure 3.30: %PDE at different pH levels of MeO dye degradation by 2 % Ni-Mn_3O_4 NPs.

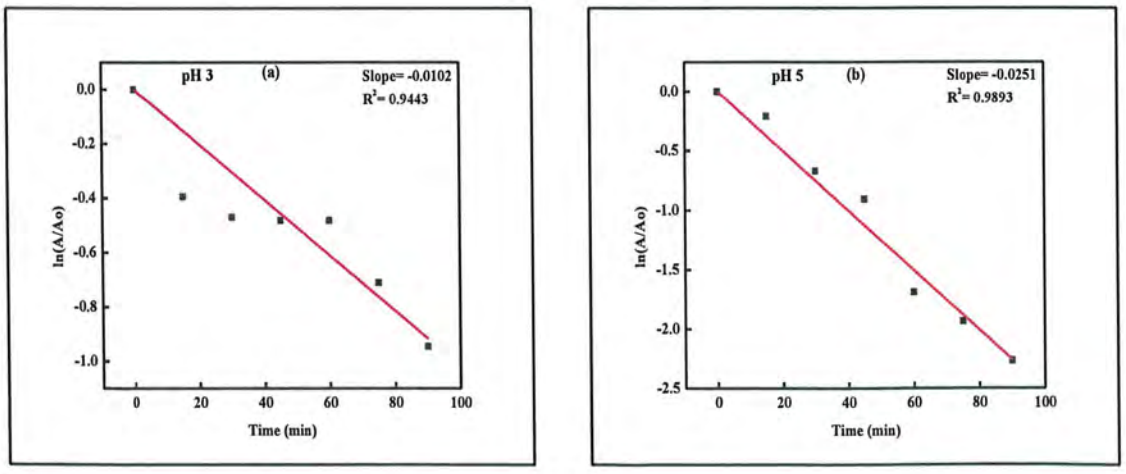

Figure 3.31: Rate constant at pH 3 and 5 for the degradation of MeO dye.

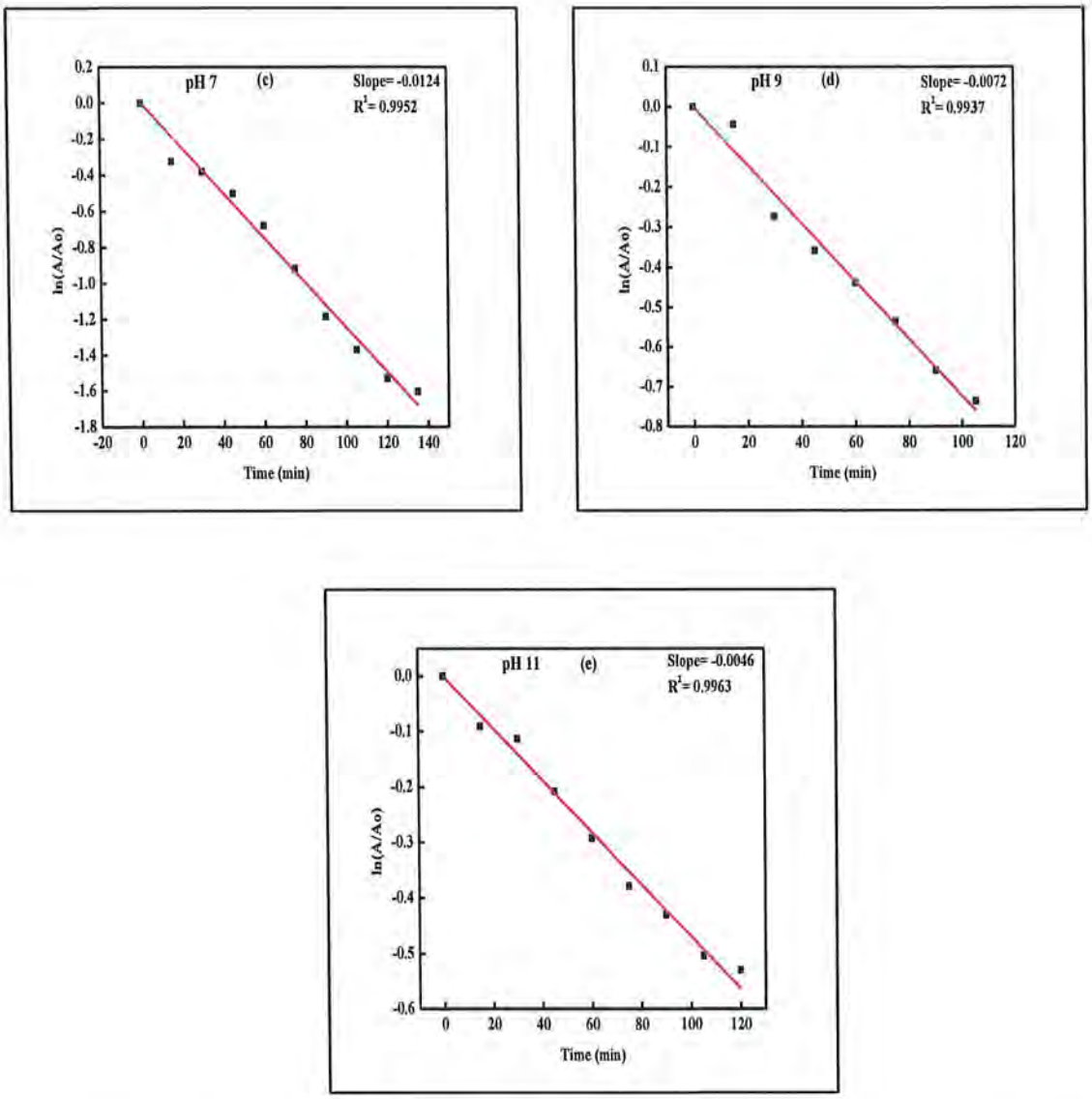

Figure 3.32: Rate constant for pH value of 7, 9 and 11 for the degradation of MeO dye.

The photocatalytic degradation of dye follows the pseudo-first order kinetics as it is confirmed from the linear fir data shown in Fig. 3.32. Table 3.11 has the half-life and kinetic data of the above synthesized material. The oxidant power of OH is inferior to holes even though hydroxyl radicals are easily produced in alkaline conditions with an abundance of hydroxyls. Consequently, under alkaline conditions, low degradation rate is obtained[69]. Fig.3.30 shows the contrast between % PDE and different pH levels

Table 3.11: Summary of pH, rate constant (k), % PDE for MeO dye, degradation by 2 % Ni-Mn_3O_4 NPs.

Sr. No.	pH	%PDE	Kinetic rate constant (min^{-1})	Half-life (min)	R^2
1	3	61.1	1.0×10^{-2}	67.94	0.9443
2	5	90.0	2.5×10^{-2}	27.60	0.9893
3	7	79.8	1.2×10^{-2}	55.88	0.9952
4	9	52.0	7.2×10^{-3}	96.25	0.9937
5	11	41.1	4.6×10^{-2}	150.65	0.9963

Conclusion

Pristine Mn_3O_4 and (1-4) % transition metal (Ni) doped Mn_3O_4 NPs were successfully synthesized followed by a co-precipitation method. The synthesized nanoparticles were characterized by using UV-Visible spectroscopy, XRD, and FT-IR analysis. UV-Visible spectroscopy indicated that with an increase in nickel percentage ranging from 1 to 3 %, an increase in the wavelength (266-285 nm) was observed and with a further increase in dopant percentage, a blue shift was observed. Tauc plots were used to find out band gaps of the synthesized nanoparticles which showed tuning in the band gap ranging from 2.50 to 2.37 eV. XRD calculations showed that the average crystallite size increases with an increasing percentage of nickel up to 3 % (12.14-14.59 nm) and after that, a decrease was calculated. There were no impurity peaks or Ni-related phases were found in XRD patterns. FT-IR analysis showed the absence of any impurity and also showed the vibration bands of the required samples. The photocatalytic degradation for Methyl blue was successfully performed under the optimal conditions of 30 μM dye concentration, 3 mg of 4 % catalyst, pH 11 & Maximum Photo Degradation Efficiency (%PDE) was 95.3 % in 75 minutes. While, the optimal condition for the degradation of Methyl orange dye was 80 μM dye concentration, 2 mg of 2 % catalyst, pH 5 & %PDE of 90 % in 90 minutes.

References

(1) Chandnani, G.; Gandhi, P.; Kanpariya, D.; Parikh, D.; Shah, M. A comprehensive analysis of contaminated groundwater: Special emphasis on nature-ecosystem and socio-economic impacts. *Groundwater Sustainable Dev.* **2022**, 100813.

(2) Niemczynowicz, J. Urban hydrology and water management–present and future challenges. *Urban Water J.* **1999**, *1* (1), 1-14.

(3) Yaseen, D.; Scholz, M. Textile dye wastewater characteristics and constituents of synthetic effluents: a critical review. *Int. J. Environ. Sci. Technol.* **2019**, *16*, 1193-1226.

(4) Mahamuni, N. N.; Adewuyi, Y. G. Advanced oxidation processes (AOPs) involving ultrasound for waste water treatment: a review with emphasis on cost estimation. *Ultrason. Sonochem.* **2010**, *17* (6), 990-1003.

(5) Harrington, W.; Krupnick, A. J.; Peskin, H. M. Policies for nonpoint-source water pollution control. *J. Soil Water Conserv.* **1985**, *40* (1), 27-32.

(6) Shen, Z.; Liao, Q.; Hong, Q.; Gong, Y. An overview of research on agricultural non-point source pollution modelling in China. *Sep. Purif. Technol.* **2012**, *84*, 104-111.

(7) Khanna, M.; Quimio, W. R. H.; Bojilova, D. Toxics release information: A policy tool for environmental protection. *J. Environ. Econ. Manage.* **1998**, *36* (3), 243-266.

(8) Kasiri, M. B.; Safapour, S. Natural dyes and antimicrobials for green treatment of textiles. *Environ. Chem. Lett.* **2014**, *12* (1), 1-13.

(9) Ezeokonkwo, M. A.; Okafor, S. N.; Godwin-Nwakwasi, E. U. Preliminary characterization of some natural dyes. *Afr. J. Pure Appl. Chem.* **2018**, *12* (7), 54-61.

(10) Bush, A. M.; Ford, H. O.; Gao, F.; Summe, M. J.; Rouvimov, S.; Schaefer, J. L.; Phillip, W. A.; Guo, R. Tunable mesoporous films from copolymers with degradable side chains as membrane precursors. *J. Membr. Sci.* **2018**, *567*, 104-114.

(11) Bernava, A. The Use of Disperse Dyes for Dyeing of Recycled Polyethylene Terephthalate Fibres. In *Key Eng. Mater.*, **2021**; Trans Tech Publ: Vol. 903, pp 100-105.

(12) Bao, P.; Dai, J. Relationships between the Solubility of CI Disperse Red 60 and Uptake on PET in Supercritical CO_2. *J. Chem. Eng. Data* **2005**, *50* (3), 838-842.

(13) Yazdanbakhsh, M.; Tavakkoli, H.; Hosseini, S. M. Characterization and evaluation catalytic efficiency of LaO. 5CaO. 5NiO_3 nanopowders in removal of reactive blue 5 from aqueous solution. *Desalin. Water Treat.* **2011**, *281*, 388-395.

(14) Khasevani, S. G.; Shahsavari, S.; Gholami, M. Green synthesis of ternary carbon dots (CDs)/MIL-88B (Fe)/Bi_2S_3 nanocomposite via MOF templating as a reusable heterogeneous nanocatalyst and nano-photocatalyst. *Mater. Res. Bull.* **2021**, *138*, 111204.

(15) Bouzikri, S.; Ouasfi, N.; Khamliche, L. Bifurcaria bifurcata activated carbon for the adsorption enhancement of Acid Orange 7 and Basic Red 5 dyes: Kinetics, equilibrium and thermodynamics investigations. *Water-Energy Nexus* **2022**, *7*, 100138.

(16) Natarajan, S.; Bajaj, H. C.; Tayade, R. J. Recent advances based on the synergetic effect of adsorption for removal of dyes from waste water using photocatalytic process. *J. Environ. Sci.* **2018**, *65*, 201-222.

(17) Belver, C.; Bedia, J.; Gómez-Avilés, A.; Peñas-Garzón, M.; Rodriguez, J. J. Semiconductor photocatalysis for water purification. In *Nanoscale Mater. Water Purif.*, Elsevier, 2019; pp 581-651.

(18) Banerjee, S.; Pillai, S. C.; Falaras, P.; O'shea, K. E.; Byrne, J. A.; Dionysiou, D. D. New insights into the mechanism of visible light photocatalysis. *J. Phys. Chem. Lett.* **2014**, *5* (15), 2543-2554.

(19) Cieśla, P.; Kocot, P.; Mytych, P.; Stasicka, Z. Homogeneous photocatalysis by transition metal complexes in the environment. *J. Mol. Catal. A: Chem.* **2004**, *224* (1-2), 17-33.

(20) Litter, M. I. Heterogeneous photocatalysis: transition metal ions in photocatalytic systems. *Appl. Catal., B* **1999**, *23* (2-3), 89-114.

(21) Mayerhöfer, T. G.; Mutschke, H.; Popp, J. Employing theories far beyond their limits—the case of the (Boguer-) beer–lambert law. *ChemPhysChem* **2016**, *17* (13), 1948-1955.

(22) Wu, Y.; Ceder, G. First principles study on Ta_3N_5:$Ti_3O_3N_2$ solid solution as a water-splitting photocatalyst. *J. Phys. Chem. C.* **2013**, *117* (47), 24710-24715.

(23) Zeng, C.; Hu, Y.; Zhang, T.; Dong, F.; Zhang, Y.; Huang, H. A core–satellite structured Z-scheme catalyst Cd 0.5 Zn 0.5 S/$BiVO_4$ for highly efficient and stable photocatalytic water splitting. *J. Mater. Chem.* **2018**, *6* (35), 16932-16942.

(24) Koe, W. S.; Lee, J. W.; Chong, W. C.; Pang, Y. L.; Sim, L. C. An overview of photocatalytic degradation: photocatalysts, mechanisms, and development of photocatalytic membrane. *Environ. Sci. Pollut. Res.* **2020**, *27*, 2522-2565.

(25) Wu, N.; Wang, J.; Tafen, D. N.; Wang, H.; Zheng, J.-G.; Lewis, J. P.; Liu, X.; Leonard, S. S.; Manivannan, A. Shape-enhanced photocatalytic activity of single-crystalline anatase TiO_2 (101) nanobelts. *J. Am. Chem. Soc.* **2010**, *132* (19), 6679-6685.

(26) Navarro Yerga, R. M.; Álvarez Galván, M. C.; Del Valle, F.; Villoria de la Mano, J. A.; Fierro, J. L. Water splitting on semiconductor catalysts under visible-light irradiation. *ChemSusChem: Chem. Sustain. Energy Mater.* **2009**, *2* (6), 471-485.

(27) Smith, A. M.; Nie, S. Semiconductor nanocrystals: structure, properties, and band gap engineering. *Acc. Chem. Res.* **2010**, *43* (2), 190-200.

(28) Satomi, K. i. Oxygen positional parameters of tetragonal Mn_3O_4. *J. Phys. Soc. Jpn.* **1961**, *16* (2), 258-266.

(29) Osgouei, M. S.; Khatamian, M.; Kakili, H. Improved visible-light photocatalytic activity of Mn_3O_4-based nanocomposites in removal of methyl orange. *Mater. Chem. Phys.* **2020**, *239*, 122108.

(30) Hu, C.-C.; Wu, Y.-T.; Chang, K.-H. Low-temperature hydrothermal synthesis of Mn_3O_4 and MnOOH single crystals: determinant influence of oxidants. *Chem. Mater.* **2008**, *20* (9), 2890-2894.

(31) Ahmed, K. A. M.; Huang, K. Formation of Mn_3O_4 nanobelts through the solvothermal process and their photocatalytic property. *Arabian J. Chem.* **2019**, *12* (3), 429-439.

(32) Anilkumar, M.; Ravi, V. Synthesis of nanocrystalline Mn3O4 at 100° C. *Mater. Res. Bull.* **2005**, *40* (4), 605-609.

(33) Raj, B. G. S.; Asiri, A. M.; Wu, J. J.; Anandan, S. Synthesis of Mn_3O_4 nanoparticles via chemical precipitation approach for supercapacitor application. *J. Alloys Compd.* **2015**, *636*, 234-240.

(34) Bastami, T. R.; Entezari, M. H. Sono-synthesis of Mn_3O_4 nanoparticles in different media without additives. *Chem. Eng. J.* **2010**, *164* (1), 261-266.

(35) Gao, W.; Ye, S.; Shao, M. Solution-combusting preparation of mono-dispersed Mn_3O_4 nanoparticles for electrochemical applications. *J. Phys. Chem. Solids* **2011**, *72* (9), 1027-1031.

(36) Chen, Z.; Lai, J.; Shek, C. Shape-controlled synthesis and nanostructure evolution of single-crystal Mn_3O_4 nanocrystals. *Scr. Mater.* **2006**, *55* (8), 735-738.

(37) Nguyen, N. T.; Chen, S.-S.; Nguyen, N. C.; Nguyen, H. T.; Tsai, H. H.; Chang, C. T. Adsorption of methyl blue on mesoporous materials using rice husk ash as silica source. *J. Nanosci. Nanotechnol.* **2016**, *16* (4), 4108-4114.

(38) Bodean, J.; Clampett, E. Lab Reporting Example.

(39) Saleh, T. A.; Gupta, V. K. Photo-catalyzed degradation of hazardous dye methyl orange by use of a composite catalyst consisting of multi-walled carbon nanotubes and titanium dioxide. *J. Colloid Interface Sci.* **2012**, *371* (1), 101-106.

(40) Devi, L. G.; Reddy, K. M. Enhanced photocatalytic activity of silver metallized TiO_2 particles in the degradation of an azo dye methyl orange: Characterization and activity at different pH values. *Appl. Surf. Sci.* **2010**, *256* (10), 3116-3121.

(41) da Silva, C. G.; Faria, J. L. s. Photochemical and photocatalytic degradation of an azo dye in aqueous solution by UV irradiation. *J. Photochem. Photobiol., A* **2003**, *155* (1-3), 133-143.

(42) Morales, G. d. V.; Sham, E. L.; Cornejo, R.; Farfan Torres, E. M. Kinetic studies of the photocalytic degradation of tartrazine. *Lat. Am. Appl. Res.* **2012**, *42* (1), 45-49.

(43) Karpagavalli, S.; Vethanathan, S. J. K.; Perumal, S. Effect of nickel doping on the structural, optical, electrochemical and magnetic properties of hausmannite (Mn_3O_4) nanoparticles. *Int. J. Nanopart.* **2019**, *11* (4), 305-321.

(44) Sukhdev, A.; Challa, M.; Narayani, L.; Manjunatha, A. S.; Deepthi, P.; Angadi, J. V.; Kumar, P. M.; Pasha, M. Synthesis, phase transformation, and morphology of hausmannite Mn_3O_4 nanoparticles: photocatalytic and antibacterial investigations. *Heliyon* **2020**, *6* (1), e03245.

(45) Brites, F.; Santana, V.; Fernandes-Machado, N. Effect of support on the photocatalytic degradation of textile effluents using Nb_2O_5 and ZnO: photocatalytic degradation of textile dye. *Top. Catal.* **2011**, *54*, 264-269.

(46) Raja, G.; Nallathambi, A.; Prakasam, A.; Gopinath, S.; Ragupathi, C.; Narayanan, S.; Tamizhdurai, P.; Kumaran, R.; Alsaiari, N. S.; Abualnaja, K. M. Effect of lattice strain on structure, morphology, electrical conductivity and magneto-optical and catalytic properties of Ni-doped Mn_3O_4 nano-crystallites synthesized by microwave route. *J. Saudi Chem. Soc.* **2022**, *26* (2), 101440.

(47) Sahoo, C.; Gupta, A. Optimization of photocatalytic degradation of methyl blue using silver ion doped titanium dioxide by combination of experimental design and response surface approach. *J. Hazard. Mater.* **2012**, *215*, 302-310.

(48) Jamali-Sheini, F.; Yousefi, R.; Bakr, N. A.; Cheraghizade, M.; Sookhakian, M.; Huang, N. M. Highly efficient photo-degradation of methyl blue and band gap shift of SnS nanoparticles under different sonication frequencies. *Mater. Sci. Semicond. Process.* **2015**, *32*, 172-178.

(49) Colina–Márquez, J.; López-Vásquez, A.; Díaz, D.; Rendón, A.; Machuca-Martínez, F. Photocatalytic treatment of a dye polluted industrial effluent with a solar pilot-scale CPC reactor. *J. Adv. Oxid. Technol.* **2009**, *12* (1), 93-99.

(50) Ma, H.; Wang, B.; Luo, X. Studies on degradation of methyl orange wastewater by combined electrochemical process. *J. Hazard. Mater.* **2007**, *149* (2), 492-498.

(51) Kuang, L.; Dong, R.; Zhang, Z.; Feng, L.; Wang, F.; Wen, Y. Hydrothermal synthesis and metal ions doping effects of single-crystal Mn_3O_4. *Mater. Res. Bull.* **2013**, *48* (9), 3122-3128.

(52) Lednev, I. K.; Ye, T.-Q.; Hester, R. E.; Moore, J. N. Femtosecond time-resolved UV− visible absorption spectroscopy of trans-azobenzene in solution. *J. Phys. Chem.* **1996**, *100* (32), 13338-13341.

(53) Holder, C. F.; Schaak, R. E. Tutorial on powder X-ray diffraction for characterizing nanoscale materials. ACS Publications: 2019; Vol. 13, pp 7359-7365.

(54) Bunaciu, A. A.; UdriŞTioiu, E. G.; Aboul-Enein, H. Y. X-ray diffraction: instrumentation and applications. *Crit. Rev. Anal. Chem.* **2015**, *45* (4), 289-299.

(55) Rozenberg, M.; Shoham, G.; Reva, I.; Fausto, R. Low-temperature Fourier transform infrared spectra and hydrogen bonding in polycrystalline L-alanine. *Spectrochim. Acta, Part A* **2003**, *59* (14), 3253-3266.

(56) Lozeman, J. J.; Führer, P.; Olthuis, W.; Odijk, M. Spectroelectrochemistry, the future of visualizing electrode processes by hyphenating electrochemistry with spectroscopic techniques. *Anal.* **2020**, *145* (7), 2482-2509.

(57) Ristić, M.; Musić, S.; Popović, S.; Dragčević, Đ.; Marciuš, M.; Ivanda, M. Synthesis and long-term phase stability of Mn_3O_4 nanoparticles. *J. Mol. Struct.* **2013**, *1044*, 255-261.

(58) Yadav, S.; Jaiswar, G. Review on undoped/doped TiO_2 nanomaterial; synthesis and photocatalytic and antimicrobial activity. *J. Chin. Chem. Soc.* **2017**, *64* (1), 103-116.

(59) Yang, Y.; Chen, X.; Feng, Y.; Yang, G. Physical mechanism of blue-shift of UV luminescence of a single pencil-like ZnO nanowire. *Nano lett.* **2007**, *7* (12), 3879-3883.

(60) Ashokkumar, M.; Muthusamy, C. Role of ionic radii and electronegativity of co-dopants (Co, Ni and Cr) on properties of Cu doped ZnO and evaluation of In-vitro cytotoxicity. *Surf. Interfaces* **2022**, *30*, 101968.

(61) Daneu, N.; Bernik, S.; Rečnik, A. Inversion boundary induced grain growth in ZnO ceramics: from atomic-scale investigations to microstructural engineering. In *J. Phys. Conf. Ser.*, 2011; IOP Publishing: Vol. 326, p 012003.

(62) El-Said, W. A.; Alsulmi, A.; Alshitari, W. Hydrothermal synthesis of Mn_3O_4 nanorods modified indium tin oxide electrode as an efficient nanocatalyst towards direct urea electrooxidation. *Plos one* **2022**, *17* (8), e0272586.

(63) Atique Ullah, A.; Fazle Kibria, A.; Akter, M.; Khan, M.; Tareq, A.; Firoz, S. H. Oxidative degradation of methylene blue using Mn 3 O 4 nanoparticles. *Water Conserv. Sci. Eng.* **2017**, *1*, 249-256.

(64) Arabi, S. M. S.; Lalehloo, R. S.; Olyai, M. R. T. B.; Ali, G. A.; Sadegh, H. Removal of congo red azo dye from aqueous solution by ZnO nanoparticles loaded on multiwall carbon nanotubes. *Physica E* **2019**, *106*, 150-155.

(65) Bharati, B.; Sonkar, A.; Singh, N.; Dash, D.; Rath, C. Enhanced photocatalytic degradation of dyes under sunlight using biocompatible TiO_2 nanoparticles. *Materials Research Express* **2017**, *4* (8), 085503.

(66) Kundu, A.; Mondal, A. Photodegradation of methylene blue under direct sunbeams by synthesized anatase titania nanoparticles. *SN Appl. Sci.* **2019**, *1*, 1-17.

(67) Peternel, I. T.; Koprivanac, N.; Božić, A. M. L.; Kušić, H. M. Comparative study of UV/TiO_2, UV/ZnO and photo-Fenton processes for the organic reactive dye degradation in aqueous solution. *J. Hazard. Mater.* **2007**, *148* (1-2), 477-484.

(68) Azad, K.; Gajanan, P. Photodegradation of methyl orange in aqueous solution by the visible light active Co: La: TiO_2 nanocomposite. *Chem. Sci. J* **2017**, *8* (3), 1000164-1000174.

(69) Chen, Y.; Liu, H.; Geng, B.; Ru, J.; Cheng, C.; Zhao, Y.; Wang, L. A reusable surface-quaternized nanocellulose-based hybrid cryogel loaded with N-doped TiO_2 for self-integrated adsorption/photo-degradation of methyl orange dye. *RSC adv.* **2017**, *7* (28), 17279-17288.